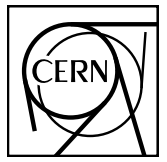


# EUROPEAN ORGANIZATION FOR NUCLEAR RESEARCH



ALICE-ANA-2016-xxx  
May 30, 2017

## Lambda-Kaon and Cascade-Kaon Femtoscopy in Pb-Pb Collisions at $\sqrt{s_{NN}} = 2.76$ TeV from the LHC ALICE Experiment

Jesse T. Buxton<sup>1</sup>

1. Department of Physics, The Ohio State University, Columbus, Ohio, USA

Email: jesse.thomas.buxton@cern.ch

### Abstract

We present results from a femtoscopic analysis of Lambda-Kaon correlations in Pb-Pb collisions at  $\sqrt{s_{NN}} = 2.76$  TeV by the ALICE experiment at the LHC. All pair combinations of  $\Lambda$  and  $\bar{\Lambda}$  with  $K^+$ ,  $K^-$  and  $K_S^0$  are analyzed. The femtoscopic correlations are the result of strong final-state interactions, and are fit with a parametrization based on a model by R. Lednicky and V. L. Lyuboshitz [1]. This allows us to both characterize the emission source and measure the scattering parameters for the particle pairs. We observe a large difference in the  $\Lambda$ - $K^+$  ( $\bar{\Lambda}$ - $K^-$ ) and  $\Lambda$ - $K^-$  ( $\bar{\Lambda}$ - $K^+$ ) correlations in pairs with low relative momenta ( $k^* \lesssim 100$  MeV). Additionally, the average of the  $\Lambda$ - $K^+$  ( $\bar{\Lambda}$ - $K^-$ ) and  $\Lambda$ - $K^-$  ( $\bar{\Lambda}$ - $K^+$ ) correlation functions is consistent with our  $\Lambda$ - $K_S^0$  ( $\bar{\Lambda}$ - $K_S^0$ ) measurement. The results suggest an effect arising from different quark-antiquark interactions in the pairs, i.e.  $s\bar{s}$  in  $\Lambda$ - $K^+$  ( $\bar{\Lambda}$ - $K^-$ ) and  $u\bar{u}$  in  $\Lambda$ - $K^-$  ( $\bar{\Lambda}$ - $K^+$ ). To gain further insight into this hypothesis, we currently are conducting a  $\Xi$ -K femtoscopic analysis.



## Contents

<b>1</b>	<b>Introduction</b>	<b>4</b>
<b>2</b>	<b>Data Sample and Software</b>	<b>4</b>
2.1	Data Sample . . . . .	4
2.2	Software . . . . .	4
<b>3</b>	<b>Data Selection</b>	<b>5</b>
3.1	Event Selection and Mixing . . . . .	5
3.2	K $^{\pm}$ Track Selection . . . . .	5
3.3	V0 Selection . . . . .	7
3.3.1	Λ Reconstruction . . . . .	7
3.3.2	K $_S^0$ Reconstruction . . . . .	9
3.4	Cascade Reconstruction . . . . .	10
3.5	Pair Selection . . . . .	12
<b>4</b>	<b>Correlation Functions</b>	<b>13</b>
<b>5</b>	<b>Fitting</b>	<b>14</b>
5.1	Model: ΛK $_S^0$ , ΛK $^{\pm}$ , Ξ $^{ch}$ K $_S^0$ . . . . .	14
5.2	Model: Ξ $^{ch}$ K $^{ch}$ . . . . .	17
5.3	Momentum Resolution Corrections . . . . .	20
5.4	Residual Correlations . . . . .	21
<b>6</b>	<b>Systematic Errors</b>	<b>24</b>
6.1	Systematic Errors: ΛK $_S^0$ . . . . .	24
6.1.1	Particle and Pair Cuts . . . . .	24
6.1.2	Non-Flat Background . . . . .	25
6.1.3	Fit Range . . . . .	26
6.2	Systematic Errors: ΛK $^{\pm}$ . . . . .	26
6.2.1	Particle and Pair Cuts . . . . .	26
6.2.2	Non-Flat Background . . . . .	26
6.2.3	Fit Range . . . . .	26
6.3	Systematic Errors: ΞK $^{\pm}$ . . . . .	26
6.3.1	Particle and Pair Cuts . . . . .	26

6.3.2	Non-Flat Background . . . . .	27
6.3.3	Fit Range . . . . .	27
<b>7</b>	<b>Results and Discussion</b>	<b>27</b>
7.1	Results: $\Lambda K_S^0$ and $\Lambda K^\pm$ . . . . .	27
7.2	Results: $\Xi K^\pm$ . . . . .	36
<b>8</b>	<b>To Do</b>	<b>36</b>

## List of Figures

1	V0 Reconstruction	7
2	$K_S^0$ contamination in $\Lambda(\bar{\Lambda})$ collection	8
3	$\Lambda$ and $\bar{\Lambda}$ Purity	9
4	$\Lambda(\bar{\Lambda})$ contamination in $K_S^0$ collection	11
5	$K_S^0$ Purity	12
6	$\Xi$ Reconstruction	12
7	$\Xi^-(\bar{\Xi}^+)$ Purity	13
8	Average Separation of $\Lambda(\bar{\Lambda})$ and $K_S^0$ Daughters	14
9	Average Separation of $\Lambda(\bar{\Lambda})$ Daughter and $K^\pm$	15
10	$\Lambda(\bar{\Lambda})K_S^0$ Correlation Functions	16
11	$\Lambda K^+$ and $\bar{\Lambda} K^-$ Correlation Functions	17
12	$\Lambda K^-$ and $\bar{\Lambda} K^+$ Correlation Functions	18
13	Correlation Functions: $\Lambda K^+$ vs $\Lambda K^-$ for 0-10% Centrality	19
14	Momentum Resolution: Sample $k_{True}^*$ vs. $k_{Rec}^*$	22
15	Particle Contaminations Visible in $k_{True}^*$ vs. $k_{Rec}^*$	23
16	Transform Matrices for $\Lambda K^+$ Analysis	24
17	Transform Matrices for $\bar{\Lambda} K^+$ Analysis	25
18	$\Lambda K_S^0(\bar{\Lambda} K_S^0)$ Fits	28
19	$\Lambda K_S^0(\bar{\Lambda} K_S^0)$ Fits (Wide Range)	29
20	$\Lambda K^+(\bar{\Lambda} K^-)$ Fits	30
21	$\Lambda K^+(\bar{\Lambda} K^-)$ Fits (Wide Range)	31
22	$\Lambda K^-(\bar{\Lambda} K^+)$ Fits	32
23	$\Lambda K^-(\bar{\Lambda} K^+)$ Fits (Wide Range)	33
24	$\Xi K^\pm$ Results	36
25	$\Xi K^\pm$ Coulomb Only	37
26	$\Xi K^\pm$ Coulomb Only	38

---

## 12 1 Introduction

13 NOTE: An updated version of this analysis note should be uploaded before 16 December 2016. Amongst  
 14 other additions, this new version will include more thorough results and discussion of our  $\Xi K^\pm$  analyses.  
 15 If possible, we would like to at least show the data from this study, and possibly even preliminary results.  
 16 However, with QM deadlines close approaching, this may not be possible.

17 We present results from a femtoscopic analysis of Lambda-Kaon correlations in Pb-Pb collisions at  $\sqrt{s_{NN}}$   
 18 = 2.76 TeV by the ALICE experiment at the LHC. All pair combinations of  $\Lambda$  and  $\bar{\Lambda}$  with  $K^+$ ,  $K^-$  and  
 19  $K_S^0$  are analyzed. The femtoscopic correlations are the result of strong final-state interactions, and are  
 20 fit with a parametrization based on a model by R. Lednický and V. L. Lyuboshitz [1]. This allows us to  
 21 both characterize the emission source and measure the scattering parameters for the particle pairs. We  
 22 observe a large difference in the  $\Lambda$ - $K^+$  ( $\bar{\Lambda}$ - $K^-$ ) and  $\Lambda$ - $K^-$  ( $\bar{\Lambda}$ - $K^+$ ) correlations in pairs with low relative  
 23 momenta ( $k^* \lesssim 100$  MeV). Additionally, the average of the  $\Lambda$ - $K^+$  ( $\bar{\Lambda}$ - $K^-$ ) and  $\Lambda$ - $K^-$  ( $\bar{\Lambda}$ - $K^+$ ) correlation  
 24 functions is consistent with our  $\Lambda$ - $K_S^0$  ( $\bar{\Lambda}$ - $K_S^0$ ) measurement. The results suggest an effect arising from  
 25 different quark-antiquark interactions in the pairs, i.e.  $s\bar{s}$  in  $\Lambda$ - $K^+$  ( $\bar{\Lambda}$ - $K^-$ ) and  $u\bar{u}$  in  $\Lambda$ - $K^-$  ( $\bar{\Lambda}$ - $K^+$ ). To  
 26 gain further insight into this hypothesis, we currently are conducting a  $\Xi$ - $K$  femtoscopic analysis.

## 27 2 Data Sample and Software

### 28 2.1 Data Sample

29 The analysis used “pass 2” reconstructed Pb-Pb data from LHC11h (AOD145). The runlist was selected  
 30 from runs with global quality tag “1” in the ALICE Run Condition Table. Approximately 40 million  
 31 combined central, semi-central, and minimum bias events were analyzed. Runs from both positive (++)  
 32 and negative (--) magnetic field polarity settings were used.

33 Run list: 170593, 170572, 170388, 170387, 170315, 170313, 170312, 170311, 170309, 170308, 170306,  
 34 170270, 170269, 170268, 170230, 170228, 170207, 170204, 170203, 170193, 170163, 170159, 170155,  
 35 170091, 170089, 170088, 170085, 170084, 170083, 170081, 170040, 170027, 169965, 169923, 169859,  
 36 169858, 169855, 169846, 169838, 169837, 169835, 169591, 169590, 169588, 169587, 169586, 169557,  
 37 169555, 169554, 169553, 169550, 169515, 169512, 169506, 169504, 169498, 169475, 169420, 169419,  
 38 169418, 169417, 169415, 169411, 169238, 169167, 169160, 169156, 169148, 169145, 169144, 169138,  
 39 169099, 169094, 169091, 169045, 169044, 169040, 169035, 168992, 168988, 168826, 168777, 168514,  
 40 168512, 168511, 168467, 168464, 168460, 168458, 168362, 168361, 168342, 168341, 168325, 168322,  
 41 168311, 168310, 168115, 168108, 168107, 168105, 168076, 168069, 167988, 167987, 167985, 167920,  
 42 167915

43 Analysis was also performed on the LHC12a17a\_fix (AOD149) Monte Carlo HIJING events for certain  
 44 checks. THERMINATOR2 was also used for certain aspects, such as transform matrices described feed-  
 45 down contributions.

### 46 2.2 Software

47 The analysis was performed on the PWGCF analysis train using AliRoot v5-08-18-1 and AliPhysics  
 48 vAN-20161027-1.

49 The main classes utilized include: AliFemtoVertexMultAnalysis, AliFemtoEventCutEstimators, AliFem-  
 50 toESDTrackCutNSigmaFilter, AliFemtoV0TrackCutNSigmaFilter, AliFemtoXiTrackCut, AliFemtoV0PairCut,  
 51 AliFemtoV0TrackPairCut, AliFemtoXiTrackPairCut, and AliFemtoAnalysisLambdaKaon. All of these  
 52 classes are contained in /AliPhysics/PWGCF/FEMTOSCOPY/AliFemto and .../AliFemtoUser.

53    **3 Data Selection**

54    **3.1 Event Selection and Mixing**

55    The events used in this study were selected with the class AliFemtoEventCutEstimators according to the  
 56    following criteria:

- 57        – Triggers
  - 58            – minimum bias (kMB)
  - 59            – central (kCentral)
  - 60            – semi-central (kSemiCentral)
- 61        – z-position of reconstructed event vertex must be within 10 cm of the center of the ALICE detector
- 62        – the event must contain at least one particle of each type from the pair of interest

63    The event mixing was handled by the AliFemtoVertexMultAnalysis class, which only mixes events with  
 64    like vertex position and centrality. The following criteria were used for event mixing:

- 65        – Number of events to mix = 5
- 66        – Vertex position bin width = 2 cm
- 67        – Centrality bin width = 5

68    The AliFemtoEventReaderAODChain class is used to read the events. Event flattening is not currently  
 69    used. FilterBit(7). The centrality is determined by the “V0M” method of AliCentrality, set by calling Al-  
 70    iFemtoEventReaderAOD::SetUseMultiplicity(kCentrality). I utilize the SetPrimaryVertexCorrectionT-  
 71    PCPoints switch, which causes the reader to shift all TPC points to be relative to the event vertex.

72    **3.2  $K^\pm$  Track Selection**

73    Charged kaons are identified using the AliFemtoESDTrackCutNSigmaFilter class. The specific cuts used  
 74    in this analysis are as follows:

75    Track Selection:

- 76        – Kinematic range:
  - 77            –  $0.14 < p_T < 1.5$
  - 78            –  $|\eta| < 0.8$
- 79        – FilterBit(7)
  - 80            – TPC tracks
- 81        – Track Quality
  - 82            – Minimum number of clusters in the TPC (fminTPCncls) = 80
  - 83            – Maximum allowed  $\chi^2/N_{DOF}$  for ITS clusters = 3.0
  - 84            – Maximum allowed  $\chi^2/N_{DOF}$  for TPC clusters = 4.0
- 85        – Primary Particle Selection:

- 86           – Maximum XY impact parameter = 2.4
- 87           – Maximum Z impact parameter = 3.0
- 88           – Remove particles with any kink labels (fRemoveKinks = true)
- 89           – Maximum allowed sigma to primary vertex (fMaxSigmaToVertex) = 3.0

90 K $^\pm$  Identification:

- 91           – PID Probabilities:
  - 92           – K: > 0.2
  - 93           –  $\pi$ : < 0.1
  - 94           –  $\mu$ : < 0.8
  - 95           – p: < 0.1
- 96           – Most probable particle type must be Kaon (fMostProbable=3)
- 97           – TPC and TOF N $_\sigma$  cuts:
  - 98           – p < 0.4 GeV/c: N $_{\sigma K, TPC}$  < 2
  - 99           – 0.4 < p < 0.45 GeV/c: N $_{\sigma K, TPC}$  < 1
  - 100           – 0.45 < p < 0.8 GeV/c: N $_{\sigma K, TPC}$  < 3 & N $_{\sigma K, TOF}$  < 2
  - 101           – 0.8 < p < 1.0 GeV/c: N $_{\sigma K, TPC}$  < 3 & N $_{\sigma K, TOF}$  < 1.5
  - 102           – p > 1.0 GeV/c: N $_{\sigma K, TPC}$  < 3 & N $_{\sigma K, TOF}$  < 1
- 103           – Electron Rejection: Reject if N $_{\sigma e-, TPC}$  < 3
- 104           – Pion Rejection: Reject if:
  - 105           – p < 0.65
    - 106           \* if TOF and TPC available: N $_{\sigma \pi, TPC}$  < 3 & N $_{\sigma \pi, TOF}$  < 3
    - 107           \* else
      - 108           · p < 0.5: N $_{\sigma \pi, TPC}$  < 3
      - 109           · 0.5 < p < 0.65: N $_{\sigma \pi, TPC}$  < 2
  - 110           – 0.65 < p < 1.5: N $_{\sigma \pi, TPC}$  < 5 & N $_{\sigma \pi, TOF}$  < 3
  - 111           – p > 1.5: N $_{\sigma \pi, TPC}$  < 5 & N $_{\sigma \pi, TOF}$  < 2

112 The purity of the K $^\pm$  collections was estimated using the MC data, for which the true identity of each  
 113 reconstructed K $^\pm$  particle is known. Therefore, the purity may be estimated as:

$$Purity(K^\pm) = \frac{N_{true}}{N_{reconstructed}} \quad (1)$$

114 Purity(K $^+$ )  $\approx$  Purity(K $^-$ )  $\approx$  97%

115 **3.3 V0 Selection**

116  $\Lambda$  ( $\bar{\Lambda}$ ) and  $K_S^0$  are neutral particles which cannot be directly detected, but must instead be reconstructed  
 117 through detection of their decay products, or daughters. This process is illustrated in Figure 1. In  
 118 general, particles which are topologically reconstructed in this fashion are called V0 particles. The  
 119 class AliFemtoV0TrackCutNSigmaFilter (which is an extension of AliFemtoV0TrackCut) is used to  
 120 reconstruct the V0s.

121 In order to obtain a true and reliable signal, one must ensure good purity of the V0 collection. The purity  
 122 of the collection is calculated as:

$$\text{Purity} = \frac{\text{Signal}}{\text{Signal} + \text{Background}} \quad (2)$$

123 To obtain both the signal and background, the invariant mass distribution ( $m_{inv}$ ) of all V0 candidates  
 124 must be constructed immediately before the final invariant mass cut. Examples of such distributions can  
 125 be found in Figures 3 and 5. It is vital that this distribution be constructed immediately before the final  
 126  $m_{inv}$  cut, otherwise it would be impossible to estimate the background. As shown in Figures 3 and 5, the  
 127 background is fit (with a polynomial) outside of the peak region of interest to obtain an estimate for the  
 128 background within the region. Within the  $m_{inv}$  cut limits, the background is the region below the fit while  
 129 the signal is the region above the fit.

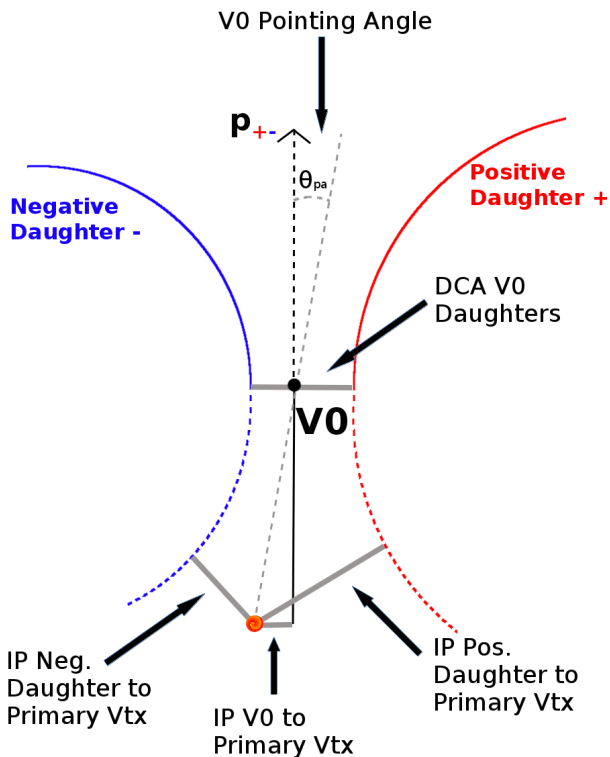


**Fig. 1:** V0 Reconstruction

130 **3.3.1  $\Lambda$  Reconstruction**

131 The following cuts were used to select good  $\Lambda$  ( $\bar{\Lambda}$ ) candidates:

- 132 1. Daughter Particle Cuts

- 133           (a) Cuts Common to Both Daughters
- 134            i.  $|\eta| < 0.8$
- 135            ii. SetTPCnclsDaughters(80)
- 136            iii. SetStatusDaughters(AliESDtrack::kTPCrefic)
- 137            iv. SetMaxDcaV0Daughters(0.4)
- 138           (b) Pion Specific Daughter Cuts
- 139            i.  $p_T > 0.16$
- 140            ii. DCA to prim vertex  $> 0.3$
- 141           (c) Proton Specific Daughter Cuts
- 142            i.  $p_T > 0.5(p) [0.3(\bar{p})] \text{ GeV}/c$
- 143            ii. DCA to prim vertex  $> 0.1$

144       2. V0 Cuts

- 145           (a)  $|\eta| < 0.8$
- 146           (b)  $p_T > 0.4$
- 147           (c)  $|m_{inv} - m_{PDG}| < 3.8 \text{ MeV}$
- 148           (d) Cosine of pointing angle  $> 0.9993$
- 149           (e) OnFlyStatus = false
- 150           (f) Decay Length  $< 60 \text{ cm}$

151       3. Shared Daughter Cut for V0 Collection

- 152           – Iterate through V0 collection to ensure that no daughter is used in more than one V0 candidate

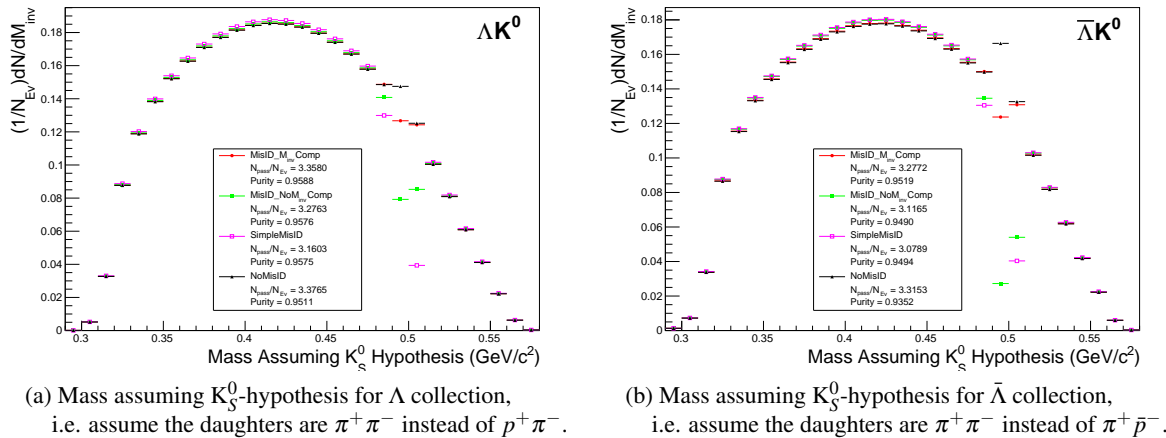


**Fig. 2:** Mass assuming  $K_S^0$ -hypothesis for V0 candidates passing all  $\Lambda$  (2a) and  $\bar{\Lambda}$  (2b) cuts. The “NoMisID” distribution (black triangles) uses the V0 finder without any attempt to remove misidentified  $K_S^0$ . The slight peak in the “NoMisID” distribution around  $m_{inv} = 0.5 \text{ GeV}/c^2$  contains misidentified  $K_S^0$  particles in our  $\Lambda(\bar{\Lambda})$  collection. “SimpleMisID” (pink squares) simply cuts out the entire peak, which throws away some good  $\Lambda$  and  $\bar{\Lambda}$  particles. “MisID\_NoM<sub>inv</sub>Comp” (green squares) uses the misidentification cut outlined in the text, but does not utilize the invariant mass comparison method. “MisID\_M<sub>inv</sub>Comp” (red circles) utilizes the full misidentification methods, and is currently used for this analysis. “ $N_{pass}/N_{ev}$ ” is the total number of  $\Lambda(\bar{\Lambda})$  particles found, normalized by the total number of events. The purity of the collection is also listed.

Figure 2a shows the mass assuming  $K_S^0$  hypothesis for the  $\Lambda$  collection, i.e. assume the daughters are  $\pi^+\pi^-$  instead of  $\pi^+\bar{p}$ . Figure 2b is a similar plot, but is for the  $\bar{\Lambda}$  collection, i.e. assume the daughters are  $\pi^+\pi^-$  instead of  $\pi^+\bar{p}$ . The  $K_S^0$  contamination is visible, although not profound, in both in the slight peaks around  $m_{inv} = 0.497 \text{ GeV}/c^2$ . If one simply cuts out the entire peak, good  $\Lambda$  particles will be lost. Ideally, the  $\Lambda$  selection and  $K_S^0$  misidentification cuts are selected such that the peak is removed from this plot while leaving the distribution continuous. To attempt to remove these  $K_S^0$  contaminations without throwing away good  $\Lambda$  and  $\bar{\Lambda}$  particles, the following misidentification cuts are imposed; a  $\Lambda(\bar{\Lambda})$  candidate is rejected if all of the following criteria are satisfied:

- $|m_{inv, K_S^0 \text{ Hypothesis}} - m_{PDG, K_S^0}| < 9.0 \text{ MeV}/c^2$
- Positive and negative daughters pass  $\pi$  daughter cut implemented for  $K_S^0$  reconstruction
- $|m_{inv, K_S^0 \text{ Hypothesis}} - m_{PDG, K_S^0}| < |m_{inv, \Lambda(\bar{\Lambda}) \text{ Hypothesis}} - m_{PDG, \Lambda(\bar{\Lambda})}|$

Figure 3 shows the invariant mass ( $M_{inv}$ ) distribution of all  $\Lambda(\bar{\Lambda})$  candidates immediately before the final invariant mass cut. These distributions are used to calculate the collection purities. The  $\Lambda$  and  $\bar{\Lambda}$  purities are found to be: Purity( $\Lambda$ )  $\approx$  Purity( $\bar{\Lambda}$ )  $\approx$  95%.

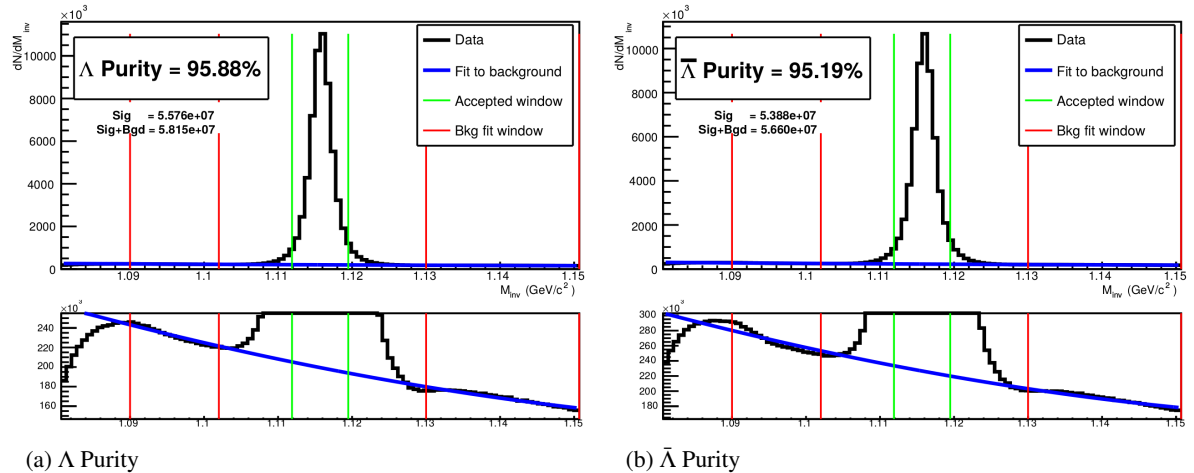


**Fig. 3:** Invariant mass ( $M_{inv}$ ) distribution of all  $\Lambda$  (a) and  $\bar{\Lambda}$  (b) candidates immediately before the final invariant mass cut. The bottom figures are zoomed to show the background with fit. The vertical green lines represent the  $M_{inv}$  cuts used in the analyses, the red vertical lines delineate the region over which the background was fit, and the blue line shows the background fit. These distributions are used to calculate the collection purities, Purity( $\Lambda$ )  $\approx$  Purity( $\bar{\Lambda}$ )  $\approx$  95%.

### 3.3.2 $K_S^0$ Reconstruction

The following cuts were used to select good  $K_S^0$  candidates:

1. Pion Daughter Cuts
  - (a)  $|\eta| < 0.8$
  - (b) SetTPCnclsDaughters(80)
  - (c) SetStatusDaughters(AliESDtrack::kTPCrefic)
  - (d) SetMaxDcaV0Daughters(0.3)

- 174                   (e)  $p_T > 0.15$   
 175                   (f) DCA to prim vertex  $> 0.3$

176       2.  $K_S^0$  Cuts

- 177                   (a)  $|\eta| < 0.8$   
 178                   (b)  $p_T > 0.2$   
 179                   (c)  $m_{PDG} - 13.677 \text{ MeV} < m_{inv} < m_{PDG} + 2.0323 \text{ MeV}$   
 180                   (d) Cosine of pointing angle  $> 0.9993$   
 181                   (e) OnFlyStatus = false  
 182                   (f) Decay Length  $< 30 \text{ cm}$

183       3. Shared Daughter Cut for V0 Collection

184           – Iterate through V0 collection to ensure that no daughter is used in more than one V0 candidate

185 As can be seen in Figure 4, some misidentified  $\Lambda$  and  $\bar{\Lambda}$  particles contaminate our  $K_S^0$  sample. Figure  
 186 4a shows the mass assuming  $\Lambda$ -hypothesis for the  $K_S^0$  collection, i.e. assume the daughters are  $p^+\pi^-$   
 187 instead of  $\pi^+\pi^-$ . Figure 4b is similar, but shows the mass assuming  $\bar{\Lambda}$  hypothesis for the collection,  
 188 i.e. assume the daughters are  $\pi^+\bar{p}^-$  instead of  $\pi^+\pi^-$ . The  $\Lambda$  contamination can be seen in 4a, and the  
 189  $\bar{\Lambda}$  contamination in 4b, in the peaks around  $m_{inv} = 1.115 \text{ GeV}/c^2$ . Additionally, the  $\bar{\Lambda}$  contamination is  
 190 visible in Figure 4a, and the  $\Lambda$  contamination visible in Figure 4b, in the region of excess around 1.65  
 191  $< m_{inv} < 2.1 \text{ GeV}/c^2$ . This is confirmed as the number of misidentified  $\Lambda$  particles in the sharp peak  
 192 of Figure 4a (misidentified  $\bar{\Lambda}$  particles in the sharp peak of Figure 4b) approximately equals the excess  
 193 found in the  $1.65 < m_{inv} < 2.1 \text{ GeV}/c^2$  region of Figure 4a (Figure 4b).

194 The peaks around  $m_{inv} = 1.115 \text{ GeV}/c^2$  in Figure 4 contain both misidentified  $\Lambda$  ( $\bar{\Lambda}$ ) particles and good  
 195  $K_S^0$ . If one simply cuts out the entire peak, some good  $K_S^0$  particles will be lost. Ideally, the  $K_S^0$  selection  
 196 and  $\Lambda(\bar{\Lambda})$  misidentification cuts can be selected such that the peak is removed from this plot while leaving  
 197 the distribution continuous. To attempt to remove these  $\Lambda$  and  $\bar{\Lambda}$  contaminations without throwing away  
 198 good  $K_S^0$  particles, the following misidentification cuts are imposed; a  $K_S^0$  candidate is rejected if all of  
 199 the following criteria are satisfied (for either  $\Lambda$  or  $\bar{\Lambda}$  hypothesis):

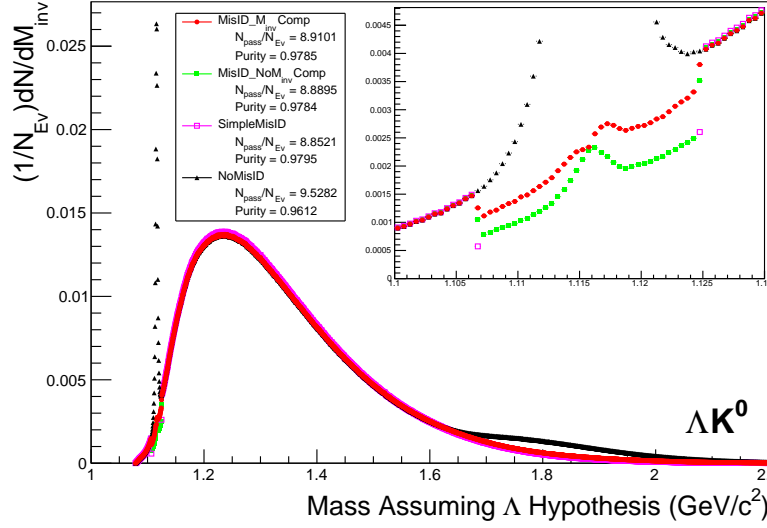
- 200           –  $|m_{inv, \Lambda(\bar{\Lambda}) \text{ Hypothesis}} - m_{PDG, \Lambda(\bar{\Lambda})}| < 9.0 \text{ MeV}/c^2$
- 201           – Positive daughter passes  $p^+(\pi^+)$  daughter cut implemented for  $\Lambda(\bar{\Lambda})$  reconstruction
- 202           – Negative daughter passes  $\pi^-(\bar{p}^-)$  daughter cut implemented by  $\Lambda(\bar{\Lambda})$  reconstruction
- 203           –  $|m_{inv, \Lambda(\bar{\Lambda}) \text{ Hypothesis}} - m_{PDG, \Lambda(\bar{\Lambda})}| < |m_{inv, K_S^0 \text{ Hypothesis}} - m_{PDG, K_S^0}|$

204       **3.4 Cascade Reconstruction**

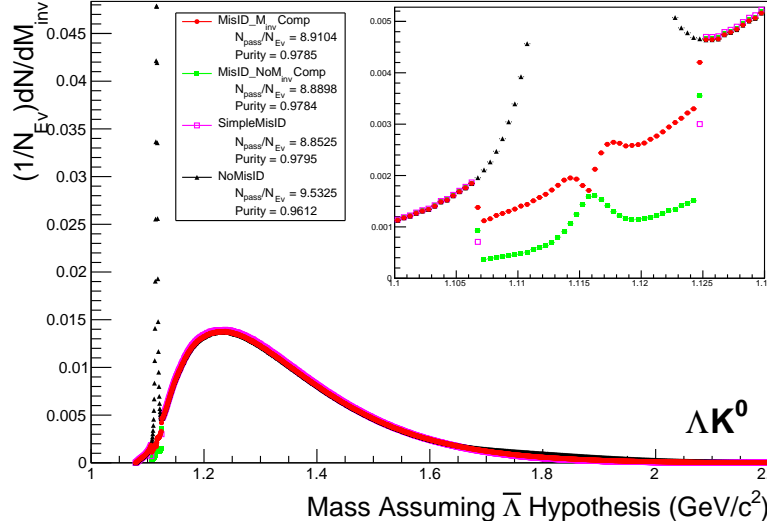
205 A description of our  $\Xi K^\pm$  analyses, as well as preliminary results and fits are expected to be uploaded by  
 206 16 December 2016.

207 Our motivation for studying  $\Xi K^\pm$  systems is to hopefully better understand the striking difference in the  
 208  $\Lambda K^+$  and  $\Lambda K^-$  data at low  $k^*$  (Figure 13).

209 The reconstruction of  $\Xi$  particles is one step above V0 reconstruction. V0 particles are topologically  
 210 reconstructed by searching for the charged daughters' tracks into which they decay. With  $\Xi$  particles, we



(a) Mass assuming  $\Lambda$ -hypothesis for  $K_S^0$  collection, i.e. assume the daughters are  $p^+ \pi^-$  instead of  $\pi^+ \pi^-$ .



(b) Mass assuming  $\bar{\Lambda}$ -hypothesis for  $K_S^0$  collection, i.e. assume the daughters are  $\pi^+ \bar{p}^-$  instead of  $\pi^+ \pi^-$ .

**Fig. 4:** Mass assuming  $\Lambda$ -hypothesis (4a) and  $\bar{\Lambda}$ -hypothesis (4b) for  $K_S^0$  collection. The “NoMisID” distribution (black triangles) uses the V0 finder without any attempt to remove misidentified  $\Lambda$  and  $\bar{\Lambda}$ . The peak in the “NoMisID” distribution around  $m_{\text{inv}} = 1.115 \text{ GeV}/c^2$  contains misidentified  $\Lambda$  (4a) and  $\bar{\Lambda}$  (4b) particles in our  $K_S^0$  collection. “SimpleMisID” (pink squares) simply cuts out the entire peak, which throws away some good  $K_S^0$  particles. “MisID\_NoM<sub>inv</sub>Comp” (green squares) uses the misidentification cut outlined in the text, but does not utilize the invariant mass comparison method. “MisID\_M<sub>inv</sub>Comp” (red circles) utilizes the full misidentification methods, and is currently used for this analysis. “ $N_{\text{pass}}/N_{\text{ev}}$ ” is the total number of  $K_S^0$  particles found, normalized by the total number of events. The purity of the collection is also listed. Also note, the relative excess of the “NoMisID” distribution around  $1.65 < m_{\text{inv}} < 2.1 \text{ GeV}/c^2$  shows misidentified  $\bar{\Lambda}$  (4a) and  $\Lambda$  (4b) particles in our  $K_S^0$  collection.

211 search for the V0 particle and charged daughter into which the  $\Xi$  decays. In the case of  $\Xi^-$ , we search  
 212 for the  $\Lambda$  (V0) and  $\pi^-$  (track) daughters. We will refer to this  $\pi$  as the “bachelor  $\pi$ ”. The reconstruction

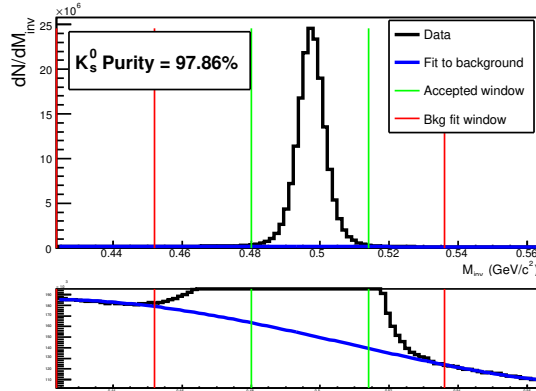


**Fig. 5:** Invariant mass ( $M_{inv}$ ) distribution of all  $K_s^0$  candidates immediately before the final invariant mass cut. The bottom figure is zoomed to show the background with fit. The vertical green lines represent the  $M_{inv}$  cut used in the analyses, the red vertical lines delineate the region over which the background was fit, and the blue line shows the background fit. This distribution is used to calculate the collection purity,  $\text{Purity}(K_s^0) \approx 98\%$ .

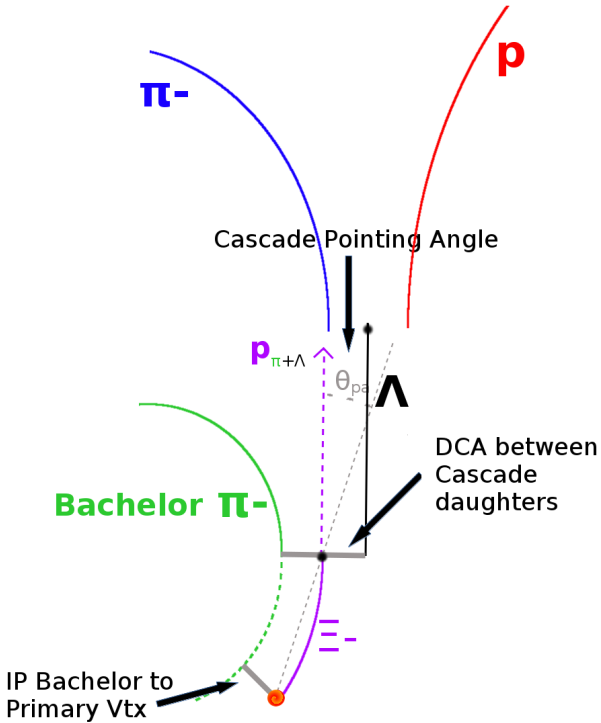


**Fig. 6:**  $\Xi$  Reconstruction

of  $\Xi$ , and the specific cuts used will be included in future versions of this note.

The purity of our  $\Xi$  and  $\bar{\Xi}$  collections are calculated just as those of our V0 collections 3.3. Figure 7, which is used to calculate the purity, shows the  $m_{inv}$  distribution of our  $\Xi(\bar{\Xi})$  candidates just before the final  $m_{inv}$  cut. Currently, we have  $\text{Purity}(\Xi^-) \approx 81\%$  and  $\text{Purity}(\bar{\Xi}^+) \approx 86\%$ .

### 3.5 Pair Selection

It is important to obtain true particle pairs in the analysis. In particular, contamination from pairs constructed with split or merged tracks, and pairs sharing daughters, can introduce an artificial signal into the correlation function, obscuring the actual physics.

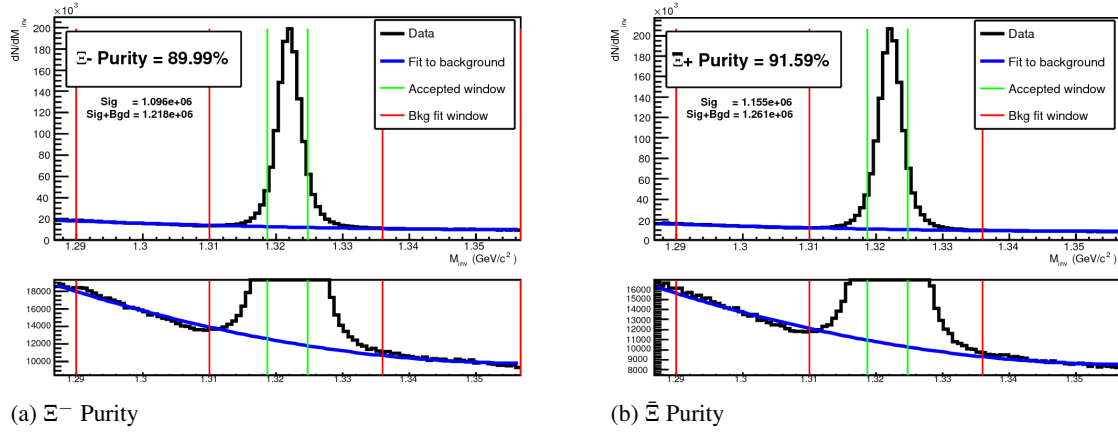


**Fig. 7:**  $\Xi^-$  ( $\bar{\Xi}^+$ ) Purity 0-10%: Purity( $\Xi^-$ )  $\approx$  90% and Purity( $\bar{\Xi}^+$ )  $\approx$  92%.

### 1. Shared Daughter Cut for Pairs

#### (a) V0-V0 Pairs (i.e. $\Lambda(\bar{\Lambda})K_S^0$ analyses)

- Remove all pairs which share a daughter
- Ex.  $\Lambda$  and  $K_S^0$  particles which share a  $\pi^-$  daughter are not included

#### (b) V0-Track Pairs (i.e. $\Lambda(\bar{\Lambda})K^\pm$ analyses)

- Remove pairs if Track is also used as a daughter of the V0
- In these analyses, this could only occur if, for instance, a  $K$  is misidentified as a  $\pi$  or  $p$  in the V0 reconstruction

### 2. Average Separation Cuts

- Used to cut out splitting and merging effects

- The motivation for these cuts can be seen in Figures 8 and 9, in which average separation correlation functions are presented

#### (a) $\Lambda(\bar{\Lambda})K_S^0$ Analyses

- Average separation  $> 6.0$  cm for like charge sign daughters
- ex.  $p$  daughter of  $\Lambda$  and  $\pi^+$  daughter of  $K_S^0$
- No cut for unlike-sign daughters

#### (b) $\Lambda(\bar{\Lambda})K^\pm$ Analyses

- Average Separation  $> 8.0$  cm for daughter of  $\Lambda(\bar{\Lambda})$  sharing charge sign of  $K^\pm$
- ex. in  $\Lambda K^+$  analysis,  $p$  daughter of  $\Lambda$  with  $K^+$
- No cut for unlike signs

## 4 Correlation Functions

This analysis studies the momentum correlations of both  $\Lambda$ -K and  $\Xi$ -K pairs using the two-particle correlation function, defined as  $C(k^*) = A(k^*)/B(k^*)$ , where  $A(k^*)$  is the signal distribution,  $B(k^*)$  is the reference (or background) distribution, and  $k^*$  is the momentum of one of the particles in the pair rest frame. In practice,  $A(k^*)$  is constructed by binning in  $k^*$  pairs from the same event. Ideally,  $B(k^*)$  is similar to  $A(k^*)$  in all respects excluding the presence of femtoscopic correlations [2]; as such,  $B(k^*)$  is used to divide out the phase-space effects, leaving only the femtoscopic effects in the correlation function.

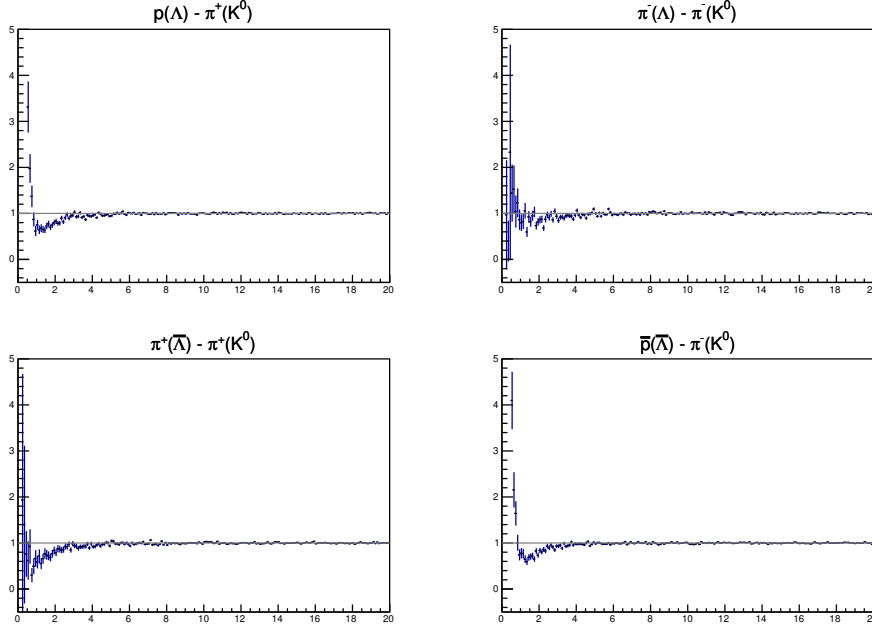


**Fig. 8:** Average separation (cm) correlation functions of  $\Lambda(\bar{\Lambda})$  and  $K_S^0$  Daughters. Only like-sign daughter pairs are shown (the distributions for unlike-signs were found to be flat). The title of each subfigure shows the daughter pair, as well as the mother of each daughter (in “( )”), ex. top left is  $p$  from  $\Lambda$  with  $\pi^+$  from  $K_S^0$ .

248 In practice,  $B(k^*)$  is obtained by forming mixed-event pairs, i.e. particles from a given event are paired  
 249 with particles from  $N_{mix}(= 5)$  other events, and these pairs are then binned in  $k^*$ . In forming the back-  
 250 ground distribution, it is important to mix only similar events; mixing events with different phase-spaces  
 251 can lead to artificial signals in the correlation function. Therefore, in this analysis, we mix events with  
 252 primary vertices within 2 cm and centralities within 5% of each other. Also note, a vertex correction is  
 253 also applied to each event, which essentially recenters the primary vertices to  $z = 0$ .

254 This analysis presents correlation functions for three centrality bins (0-10%, 10-30%, and 30-50%),  
 255 and is currently pair transverse momentum ( $k_T = 0.5|\mathbf{p}_{T,1} + \mathbf{p}_{T,2}|$ ) integrated (i.e. not binned in  $k_T$ ).  
 256 The correlation functions are constructed separately for the two magnetic field configurations, and are  
 257 combined using a weighted average:

$$C_{combined}(k^*) = \frac{\sum_i w_i C_i(k^*)}{\sum_i w_i} \quad (3)$$

258 where the sum runs over the correlation functions to be combined, and the weight,  $w_i$ , is the number of  
 259 numerator pairs in  $C_i(k^*)$ . Here, the sum is over the two field configurations.

260 Figures 10, 11, and 12 show the correlation functions for all centralities studied for  $\Lambda K_S^0(\bar{\Lambda} K_S^0)$ ,  $\Lambda K^+(\bar{\Lambda} K^-)$ ,  
 261 and  $\Lambda K^-(\bar{\Lambda} K^+)$ , respectively. All were normalized in the range  $0.32 < k^* < 0.4$  GeV/c.

## 262 5 Fitting

### 263 5.1 Model: $\Lambda K_S^0$ , $\Lambda K^\pm$ , $\Xi^{ch} K_S^0$

264 In the absence of Coulomb effects, and assuming a spherically gaussian source of width  $R$ , the 1D  
 265 femtoscopic correlation function can be calculated analytically using:

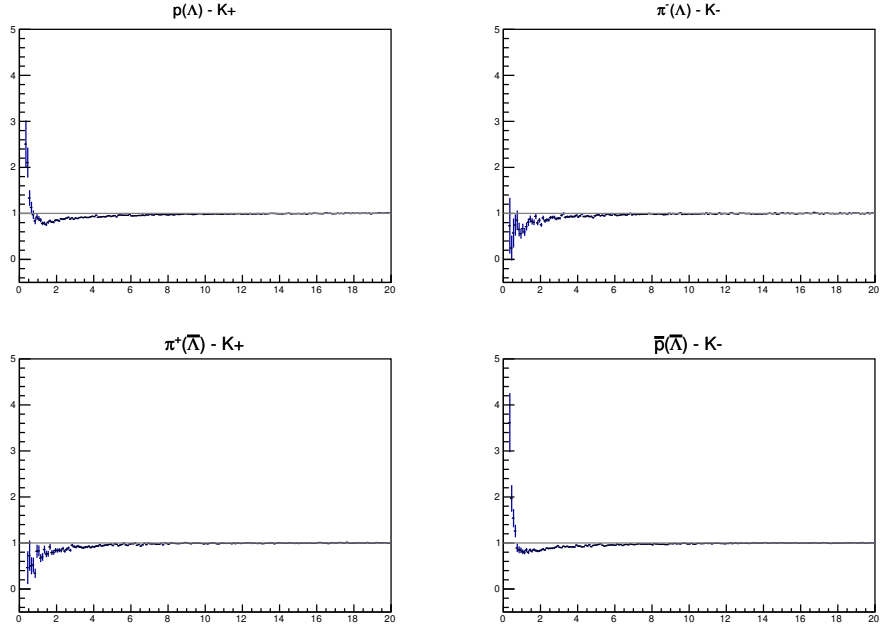


**Fig. 9:** Average separation (cm) correlation functions of  $\Lambda(\bar{\Lambda})$  Daughter and  $K^\pm$ . Only like-sign pairs are shown (unlike-signs were flat). In the subfigure titles, the particles in “( )” represent the mothers, ex. top left is  $p$  from  $\Lambda$  with  $K^+$ .

$$C(k^*) = 1 + \lambda [C_{QI}(k^*) + C_{FSI}(k^*)] \quad (4)$$

266  $C_{QI}$  describes plane-wave quantum interference:

$$C_{QI}(k^*) = \alpha \exp(-4k^{*2}R^2) \quad (5)$$

267 where  $\alpha = (-1)^{2j}/(2j+1)$  for identical particles with spin  $j$ , and  $\alpha = 0$  for non-identical particles.  
268 Obviously,  $\alpha = 0$  for all analyses presented in this note.  $C_{FSI}$  describes the s-wave strong final state  
269 interaction between the particles:

$$C_{FSI}(k^*) = (1 + \alpha) \left[ \frac{1}{2} \left| \frac{f(k^*)}{R} \right|^2 \left( 1 - \frac{d_0}{2\sqrt{\pi}R} \right) + \frac{2\Re f(k^*)}{\sqrt{\pi}R} F_1(2k^*R) - \frac{\Im f(k^*)}{R} F_2(2k^*R) \right] \quad (6)$$

$$f(k^*) = \left( \frac{1}{f_0} + \frac{1}{2} d_0 k^{*2} - ik^* \right)^{-1}; \quad F_1(z) = \int_0^z \frac{e^{x^2-z^2}}{z} dx; \quad F_2(z) = \frac{1-e^{-z^2}}{z}$$

270 where  $R$  is the source size,  $f(k^*)$  is the s-wave scattering amplitude,  $f_0$  is the complex scattering length,  
271 and  $d_0$  is the effective range of the interaction.

272 The code developed to fit the data is called “LednickýFitter”, and utilizes the ROOT TMinuit implemen-  
273 tation of the MINUIT fitting package. In short, given a function with a number of parameters, the fitter  
274 explores the parameter space searching for the minimum of the equation. In this implementation, the  
275 function to be minimized should represent the difference between the measure and theoretical corre-  
276 lation functions. However, a simple  $\chi^2$  test is inappropriate for fitting correlation functions, as the ratio  
277 two Poisson distributions does not result in a Poisson distribution. Instead, a log-likelihood fit function  
278 of the following form is used [2]:

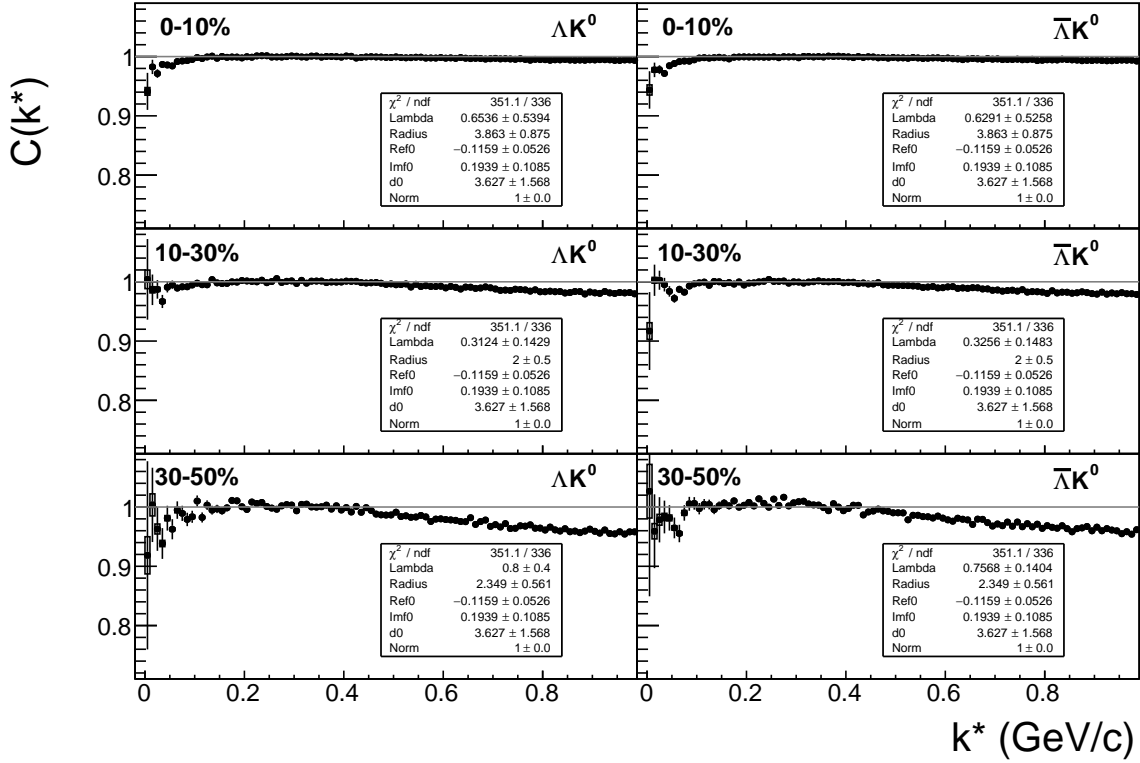


**Fig. 10:**  $\Lambda K_S^0$  (left) and  $\bar{\Lambda} K_S^0$  (right) correlation functions for 0-10% (top), 10-30% (middle), and 30-50% (bottom) centralities. The lines represent the statistical errors, while the boxes represent the systematic errors.

$$\chi_{PML}^2 = -2 \left[ A \ln \left( \frac{C(A+B)}{A(C+1)} \right) + B \ln \left( \frac{A+B}{B(C+1)} \right) \right] \quad (7)$$

where  $A$  is the experimental signal distribution (numerator),  $B$  is the experimental background distribution (denominator), and  $C$  is the theoretical fit correlation function.

The LednickyFitter uses Equations 4 – 6 to build the theoretical fit, and Equation 7 as the statistic quantifying the quality of the fit. The parameters to be varied by MINUIT are:  $\lambda$ ,  $R$ ,  $f_0$  ( $\mathbb{R}f_0$  and  $\mathbb{I}f_0$  separately),  $d_0$ , and normalization  $N$ . The fitter currently includes methods to correct for momentum resolution and a non-flat background. These corrections are applied to the fit function, the data is never touched. The fitter is able to share parameters between different analyses and fit all simultaneously.

In a typical fit, a given pair is fit with its conjugate (ex.  $\Lambda K^+$  with  $\bar{\Lambda} K^-$ ) across all centralities (0-10%, 10-30%, 30-50%), for a total of 6 simultaneous analyses. Each analysis has a unique  $\lambda$  and normalization parameter. The radii are shared between analyses of like centrality, as these should have similar source sizes. The scattering parameters ( $\mathbb{R}f_0$ ,  $\mathbb{I}f_0$ ,  $d_0$ ) are shared amongst all.

Figures 18, 20, and 22 (Section 7) show experimental data with fits for all studied centralities for  $\Lambda K_S^0$  with  $\bar{\Lambda} K_S^0$ ,  $\Lambda K^+$  with  $\bar{\Lambda} K^-$ , and  $\Lambda K^-$  with  $\bar{\Lambda} K^+$ , respectively. In the figures, the black solid line represents the “raw” fit, i.e. not corrected for momentum resolution effects nor non-flat background. The green line shows the fit to the non-flat background. The purple points show the fit after momentum resolution and non-flat background corrections have been applied. The initial values of the parameters is listed, as well as the final fit values with uncertainties.

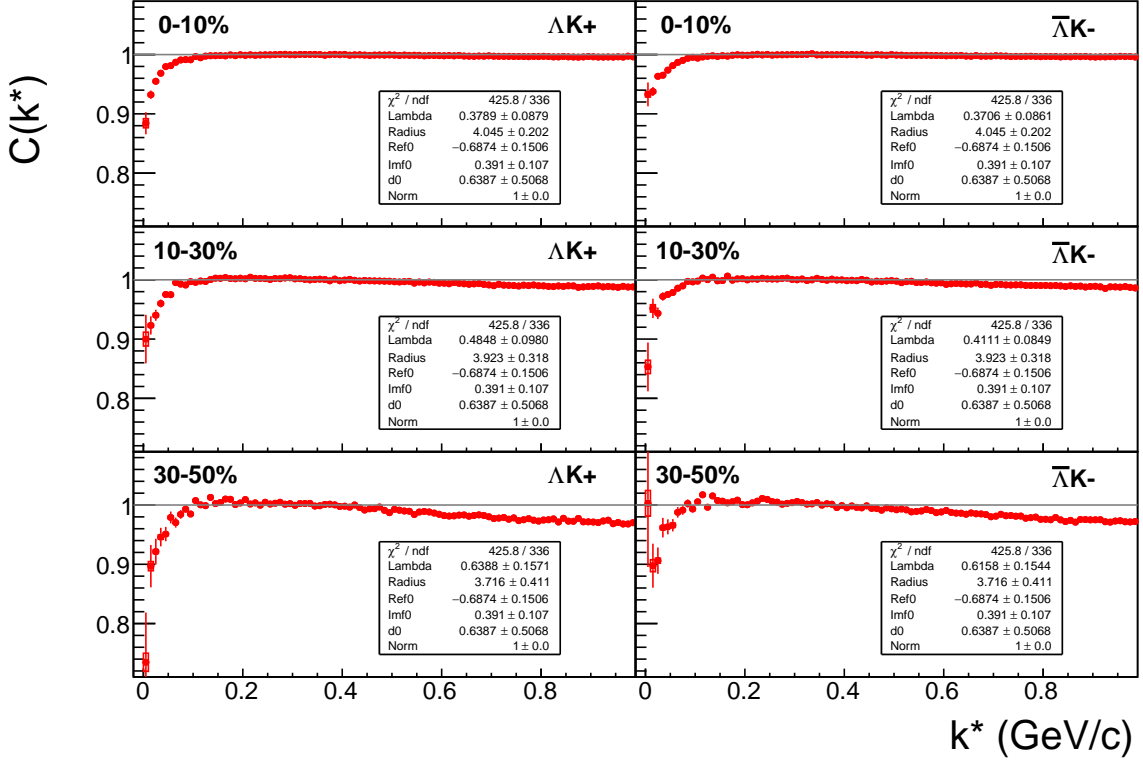


**Fig. 11:**  $\Lambda K^+$  (left) and  $\bar{\Lambda} K^-$  (right) correlation functions for 0-10% (top), 10-30% (middle), and 30-50% (bottom) centralities. The lines represent the statistical errors, while the boxes represent the systematic errors.

## 296 5.2 Model: $\Xi^{ch} K^{ch}$

297 When fitting the  $\Xi^-(\bar{\Xi}^+)K^\pm$  results, it is necessary to include both strong and Coulomb effects. In this  
298 case, Equation 4 is no longer valid, and, in fact, there is no analytical form with which to fit. Therefore,  
299 we must begin with the wave function describing the pair interaction, and simulate many particle pairs  
300 to obtain a theoretical fit correlation function. The code developed to achieve this functionality is called  
301 “CoulombFitter”. Currently, in order to generate the statistics needed for a stable fit, we find that  $\sim 10^4$   
302 simulated pairs per 10 MeV bin are necessary. Unfortunately, the nature of this process means that the  
303 “CoulombFitter” takes much longer to run than the “LednickyFitter” of Section 5.1.

304 The two-particle correlation function may be written as:

$$C(\mathbf{k}^*) = \sum_S \rho_S \int S(\mathbf{r}^*) |\Psi_{\mathbf{k}^*}^S(\mathbf{r}^*)|^2 d^3 \mathbf{r}^* \quad (8)$$

305 where  $\rho_S$  is the normalized emission probability of particles in a state with spin  $S$ ,  $S(\mathbf{r}^*)$  is the pair  
306 emission source distribution (assumed to be Gaussian), and  $\Psi_{\mathbf{k}^*}^S(\mathbf{r}^*)$  is the two-particle wave-function  
307 including both strong and Coulomb interactions [3]:

$$\Psi_{\mathbf{k}^*}(\mathbf{r}^*) = e^{i\delta_c} \sqrt{A_c(\eta)} [e^{i\mathbf{k}^* \cdot \mathbf{r}^*} F(-i\eta, 1, i\xi) + f_c(k^*) \frac{\tilde{G}(\rho, \eta)}{r^*}] \quad (9)$$

308 where  $\rho = k^* r^*$ ,  $\eta = (k^* a_c)^{-1}$ ,  $\xi = \mathbf{k}^* \cdot \mathbf{r}^* + k^* r^* \equiv \rho(1 + \cos \theta^*)$ , and  $a_c = (\mu z_1 z_2 e^2)^{-1}$  is the two-  
309 particle Bohr radius (including the sign of the interaction).  $\delta_c$  is the Coulomb s-wave phase shift,  $A_c(\eta)$

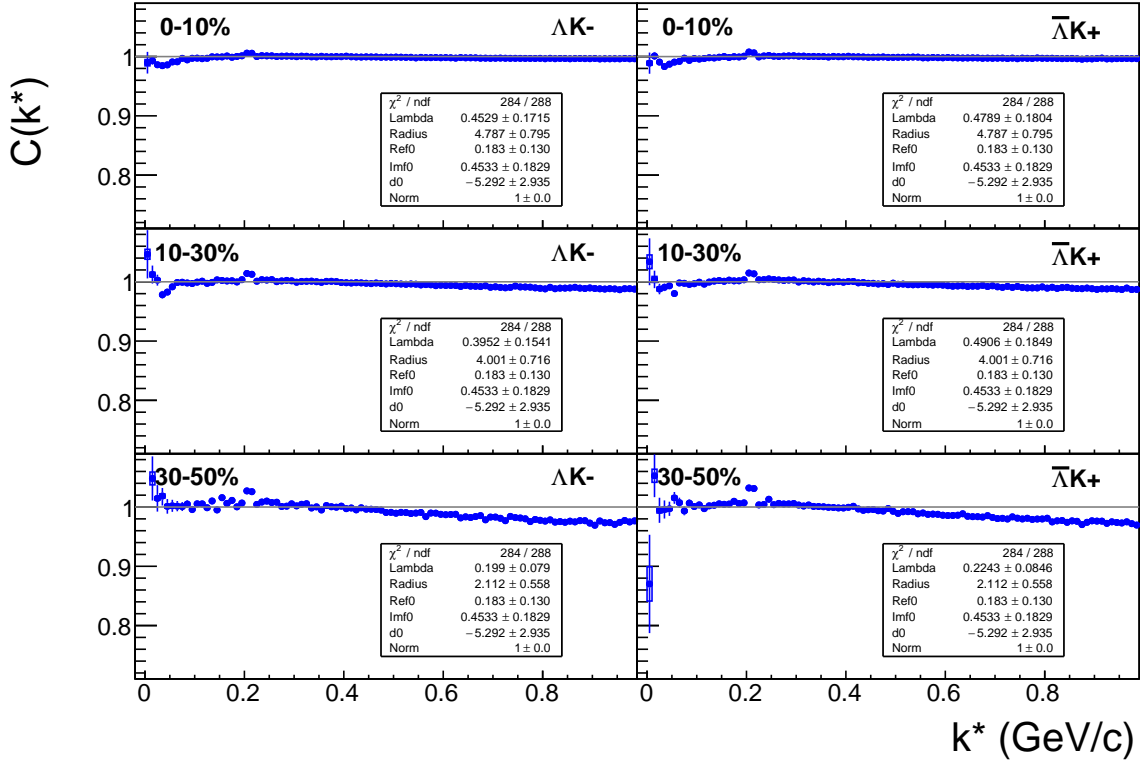


**Fig. 12:**  $\Lambda K^-$  (left) and  $\bar{\Lambda} K^+$  (right) correlation functions for 0-10% (top), 10-30% (middle), and 30-50% (bottom) centralities. The lines represent the statistical errors, while the boxes represent the systematic errors. The peak at  $k^* \approx 0.2$  GeV/c is due to the  $\Omega^-$  resonance.

is the Coulomb penetration factor,  $\tilde{G} = \sqrt{A_c}(G_0 + iF_0)$  is a combination of the regular ( $F_0$ ) and singular ( $G_0$ ) s-wave Coulomb functions.  $f_c(k^*)$  is the s-wave scattering amplitude:

$$f_c(k^*) = \left[ \frac{1}{f_0} + \frac{1}{2} d_0 k^{*2} - \frac{2}{a_c} h(\eta) - ik^* A_c(\eta) \right]^{-1} \quad (10)$$

where, the “h-function”,  $h(\eta)$ , is expressed through the digamma function,  $\psi(z) = \Gamma'(z)/\Gamma(z)$  as:

$$h(\eta) = 0.5[\psi(i\eta) + \psi(-i\eta) - \ln(\eta^2)] \quad (11)$$

As stated before, to generate a fit correlation function, we must simulate a large number of pairs, calculate the wave-function, and average  $\Psi^2$  over all pairs in a given  $k^*$  bin. Essentially, we calculate Equation 8 by hand:

$$\begin{aligned} C(\mathbf{k}^*) &= \sum_S \rho_S \int S(\mathbf{r}^*) |\Psi_{\mathbf{k}^*}^S(\mathbf{r}^*)|^2 d^3 \mathbf{r}^* \\ &\longrightarrow C(|\mathbf{k}^*|) \equiv C(k^*) = \sum_S \rho_S \langle |\Psi^S(\mathbf{k}_i^*, \mathbf{r}_i^*)|^2 \rangle_i \\ &\longrightarrow C(k^*) = \lambda \sum_S \rho_S \langle |\Psi^S(\mathbf{k}_i^*, \mathbf{r}_i^*)|^2 \rangle_i + (1 - \lambda) \end{aligned} \quad (12)$$

where  $\langle \rangle_i$  represents an average over all pairs in a given  $k^*$  bin.

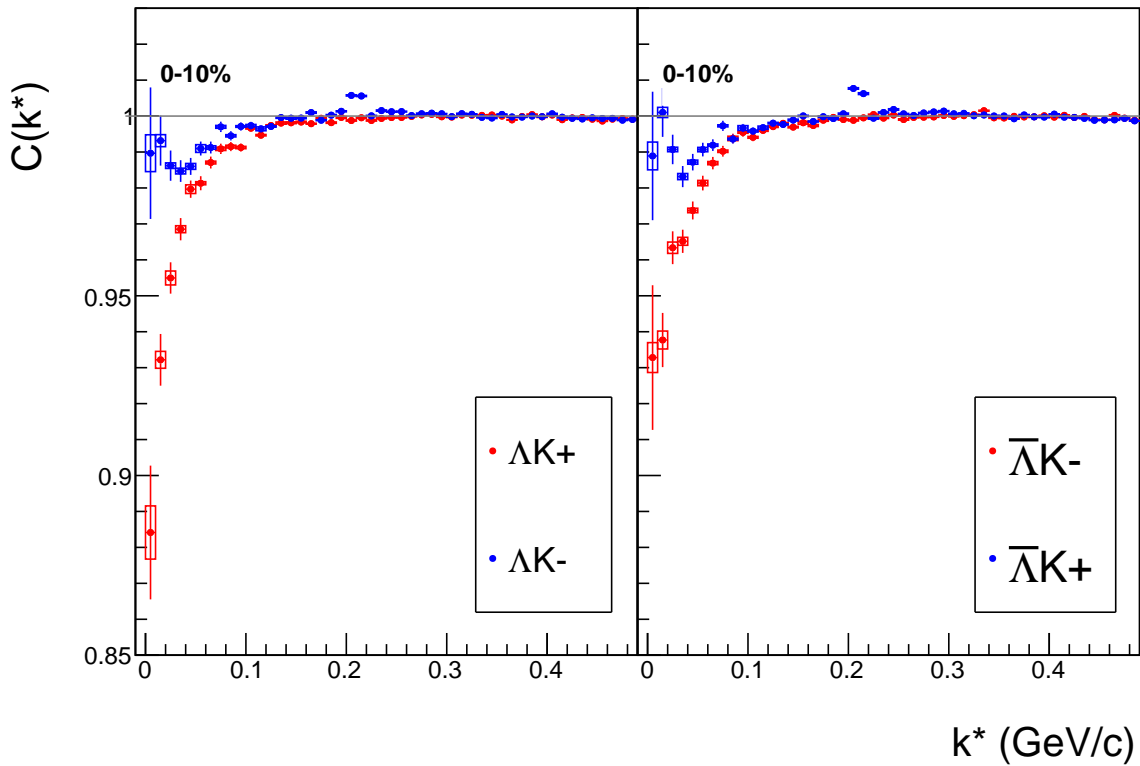


**Fig. 13:** Correlation Functions:  $\Lambda K^+$  vs  $\Lambda K^-$  ( $\bar{\Lambda} K^+$  vs  $\bar{\Lambda} K^-$ ) for 0-10% centrality. The peak in  $\Lambda K^-$  ( $\bar{\Lambda} K^+$ ) at  $k^* \approx 0.2 \text{ GeV}/c$  is due to the  $\Omega^-$  resonance. The lines represent the statistical errors. (NOTE: This figure is slightly dated, and a new one will be generated which includes both statistical and systematic uncertainties)

317 In summary, for a given  $k^*$  bin, we must draw  $N_{\text{pairs}} \sim 10^4$  pairs, and for each pair:

318 1. Draw a random  $\mathbf{r}^*$  vector according to our Gaussian source distribution  $S(\mathbf{r}^*)$

319 2. Draw a random  $\mathbf{k}^*$  vector satisfying the  $|k^*|$  restriction of the bin

320 – We draw from real  $k^*$  vectors obtained from the data

321 – However, we find that drawing from a distribution flat in  $k^*$  gives similar results

322 3. Construct the wave-function  $\Psi$

323 After all pairs for a given  $k^*$  bin are simulated and wave-functions obtained, the results are averaged to  
324 give the fit result.

325 Construction of the wave-functions, Equation 9, involves a number of complex functions not included  
326 in standard C++ or ROOT libraries (namely,  $h(\eta)$ ,  $\tilde{G}(\rho, \eta)$ , and  $F(-i\eta, 1, i\xi)$ ). These functions were  
327 even difficult to find and implement from elsewhere. Our solution was to embed a Mathematica kernel  
328 into our C++ code to evaluate these functions. However, having Mathematica work on-the-fly with the  
329 fitter was far too time consuming (fitter would have taken day, maybe weeks to finish). Our solution  
330 was to use Mathematica to create matrices representing these functions for different parameter values.  
331 During fitting, these matrices were then interpolated and the results used to build the wave-functions.  
332 This method decreased the running time dramatically, and we are not able to generate results in under  $\sim$   
333 1 hour. This process will be explained in more detail in future versions of the note.

334 **5.3 Momentum Resolution Corrections**

335 Finite track momentum resolution causes the reconstructed momentum of a particle to smear around the  
 336 true value. This, of course, also holds true for V0 particles. The effect is propagated up to the pairs  
 337 of interest, which causes the reconstructed relative momentum ( $k_{Rec}^*$ ) to differ from the true momentum  
 338 ( $k_{True}^*$ ). Smearing of the momentum typically will result in a suppression of the signal.

339 The effect of finite momentum resolution can be investigated using the MC data, for which both the true  
 340 and reconstructed momenta are available. Figure 14 shows sample  $k_{True}^*$  vs.  $k_{Rec}^*$  plots for  $\Lambda(\bar{\Lambda})K^\pm$  0-  
 341 10% analyses; Figure 14a was generated using same-event pairs, while Figure 14b was generated using  
 342 mixed-event pairs (with  $N_{mix} = 5$ ).

343 If there are no contaminations in our particle collection, the plots in Figure 14 should be smeared around  
 344  $k_{True}^* = k_{Rec}^*$ ; this is mostly true in our analyses. However, there are some interesting features of our results  
 345 which demonstrate a small (notice the log-scale on the z-axis) contamination in our particle collection.  
 346 The structure around  $k_{Rec}^* = k_{True}^* - 0.15$  is mainly caused by  $K_S^0$  contamination in our  $\Lambda(\bar{\Lambda})$  sample. The  
 347 remaining structure not distributed about  $k_{Rec}^* = k_{True}^*$  is due to  $\pi$  and  $e$  contamination in our  $K^\pm$  sample.  
 348 These contaminations are more visible in Figure 15, which show  $k_{Rec}^*$  vs.  $k_{True}^*$  plots (for a small sample  
 349 of the  $\Lambda K^\pm$  0-10% central analysis), for which the MC truth (i.e. true, known identity of the particle)  
 350 was used to eliminate misidentified particles in the  $K^+(a)$  and  $\Lambda(b)$  collections. (NOTE: This is an old  
 351 figure and is for a small sample of the data. A new version will be generated shortly. It, nonetheless,  
 352 demonstrates the point well).

353 Information gained from looking at  $k_{Rec}^*$  vs  $k_{True}^*$  can be used to apply corrections to account for the  
 354 effects of finite momentum resolution on the correlation functions. A typical method involves using the  
 355 MC HIJING data to build two correlation functions,  $C_{Rec}(k^*)$  and  $C_{True}(k^*)$ , using the generator-level  
 356 momentum ( $k_{True}^*$ ) and the measured detector-level momentum ( $k_{Rec}^*$ ). The data is then corrected by  
 357 multiplying by the ratio,  $C_{True}/C_{Rec}$ , before fitting. This essentially unsmears the data, which that can  
 358 be compared directly to theoretical predictions and fits. Although this is conceptually simple, there are  
 359 a couple of big disadvantages to this method. First, HIJING does not incorporate final-state interactions,  
 360 so weights must be used when building same-event (numerator) distributions. These weights account for  
 361 the interactions, and, in the absence of Coulomb interactions, can be calculated using Eq. 4. Of course,  
 362 these weights are valid only for a particular set of fit parameters. Therefore, in the fitting process, during  
 363 which the fitter explores a large parameter set, the corrections will not remain valid. As such, applying  
 364 the momentum resolution correction and fitting becomes a long and drawn out iterative process. An initial  
 365 parameter set is obtained (through fitting without momentum resolution corrections, theoretical models,  
 366 or a good guess), then the MC data is run over to obtain the correction factor, the data is fit using the  
 367 correction factor, a refined parameter set is extracted, the MC data is run over again to obtain the new  
 368 correction factor, etc. This process continues until the parameter set stabilizes. The second issue concerns  
 369 statistics. With the MC data available on the grid, we were not able to generate the statistics necessary  
 370 to use the raw  $C_{True}/C_{Rec}$  ratio. The ratio was not stable, and when applied to the data, obscured the  
 371 signal. Attempting to fit the ratio to generate the corrections also proved problematic. However, as  
 372 HIJING does not include final-state interactions, the same-event and mixed-event pairs are very similar  
 373 (with the exception of things like energy and momentum conservation, etc). Therefore, one may build  
 374 the numerator distribution using mixed-event pairs. This corresponds, more or less, to simply running a  
 375 the weight generator through the detector framework.

376 A second approach is to use information gained from plots like those in Figure 14, which can be considered  
 377 response matrices. The response matrix describes quantitatively how each  $k_{Rec}^*$  bin receives contributions  
 378 from multiple  $k_{True}^*$  bins, and can be used to account for the effects of finite momentum resolution.  
 379 With this approach, the resolution correction is applied on-the-fly during the fitting process by propagating  
 380 the theoretical (fit) correlation function through the response matrix, according to:

$$C_{fit}(k_{Rec}^*) = \frac{\sum_{k_{True}^*} M_{k_{Rec}^*, k_{True}^*} C_{fit}(k_{True}^*)}{\sum_{k_{True}^*} M_{k_{Rec}^*, k_{True}^*}} \quad (13)$$

where  $M_{k_{Rec}^*, k_{True}^*}$  is the response matrix (Figure 14),  $C_{fit}(k_{True}^*)$  is the fit binned in  $k_{True}^*$ , and the denominator normalizes the result.

Equation 13 describes that, for a given  $k_{Rec}^*$  bin, the observed value of  $C(k_{Rec}^*)$  is a weighted average of all  $C(k_{True}^*)$  values, where the weights are the normalized number of counts in the  $[k_{Rec}^*, k_{True}^*]$  bin. As seen in Figure 14, overwhelmingly the main contributions comes from the  $k_{Rec}^* = k_{True}^*$  bins. Although the correction is small, it is non-negligible for the low- $k^*$  region of the correlation function.

Here, the momentum resolution correction is applied to the fit, not the data. In other words, during fitting, the theoretical correlation function is smeared just as real data would be, instead of unsmearing the data. This may not be ideal for the theorist attempting to compare a model to experimental data, but it leaves the experimental data unadulterated. The current analyses use this second approach to applying momentum resolution corrections because of two major advantages. First, the MC data must be analyzed only once, and no assumptions about the fit are needed. Secondly, the momentum resolution correction is applied on-the-fly by the fitter, delegating the iterative process to a computer instead of the user.

#### 5.4 Residual Correlations

The purpose of this analysis is study the interaction and scale of the emitting source of the pairs. In order to obtain correct results, it is important for our particle collections to consist of primary particles. In practice, this is difficult to achieve for our  $\Lambda$  and  $\bar{\Lambda}$  collections. Many of our  $\Lambda$  particles are not primary, but originate as decay products from other hyperons, including  $\Sigma^0$ ,  $\Xi^-$ ,  $\Xi^0$  and  $\Omega^-$ . In these decays, the  $\Lambda$  carries away a momentum very similar to that of its parent. As a result, the correlation function between a secondary  $\Lambda$  and, for instance, a  $K^+$  will be sensitive to, and dependent upon, the interaction between the parent of the  $\Lambda$  and the  $K^+$ . In effect, the correlation between the parent of the  $\Lambda$  and the  $K^+$  (ex.  $\Sigma^0 K^+$ ) will be visible, although smeared out, in the  $\Lambda K^+$  data. We call this a residual correlation resulting from feed-down.

As it is difficult for us to eliminate these residual correlations in our analyses, we must attempt to account for them in our fitter. To achieve this, we will simultaneously fit the data for both the primary correlation function and the residual correlations. For example, in the simple case of a  $\Lambda K^+$  analysis with residuals arising solely from  $\Sigma^0 K^+$  feed-down:

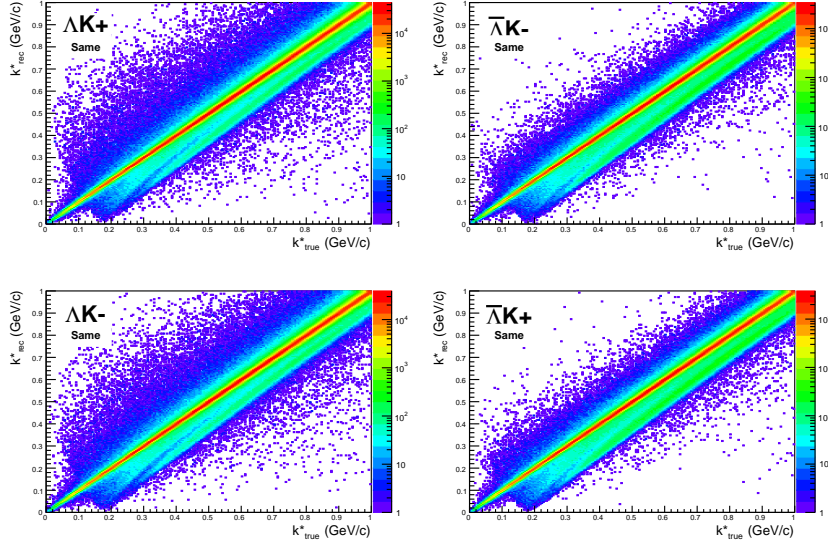
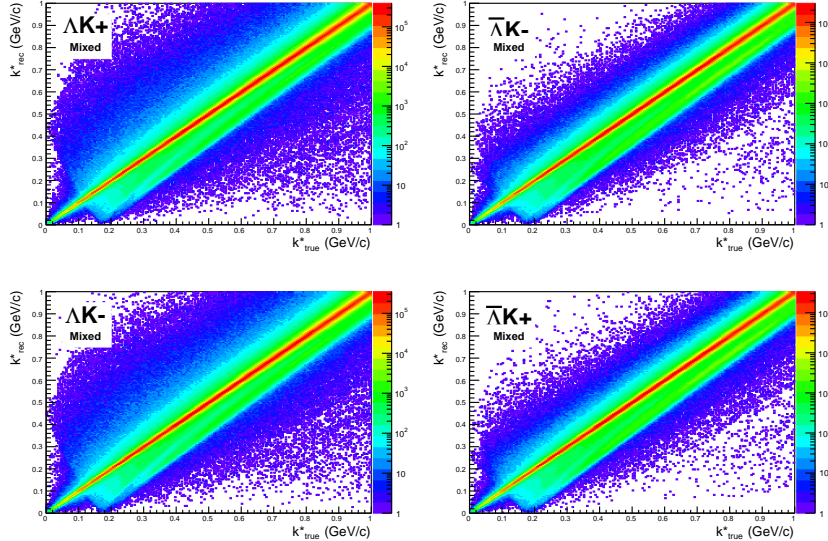
$$C_{measured}(k_{\Lambda K^+}^*) = 1 + \lambda_{\Lambda K^+} [C_{\Lambda K^+}(k_{\Lambda K^+}^*) - 1] + \lambda_{\Sigma^0 K^+} [C_{\Sigma^0 K^+}(k_{\Lambda K^+}^*) - 1]$$

$$C_{\Sigma^0 K^+}(k_{\Lambda K^+}^*) \equiv \sum_{k_{\Sigma^0 K^+}^*} \frac{C_{\Sigma^0 K^+}(k_{\Sigma^0 K^+}^*) T(k_{\Sigma^0 K^+}^*, k_{\Lambda K^+}^*)}{T(k_{\Sigma^0 K^+}^*, k_{\Lambda K^+}^*)} \quad (14)$$

$C_{\Sigma^0 K^+}(k_{\Sigma^0 K^+}^*)$  is the  $\Sigma^0 K^+$  correlation function from, for instance, Equation 4, and  $T$  is the transform matrix generated with THERMINATOR. This equation can be easily extended to include feed-down from more sources:

$$C_{measured}(k_{\Lambda K}^*) = \sum_i \lambda_i C_i(k_{\Lambda K}^*) \quad (15)$$

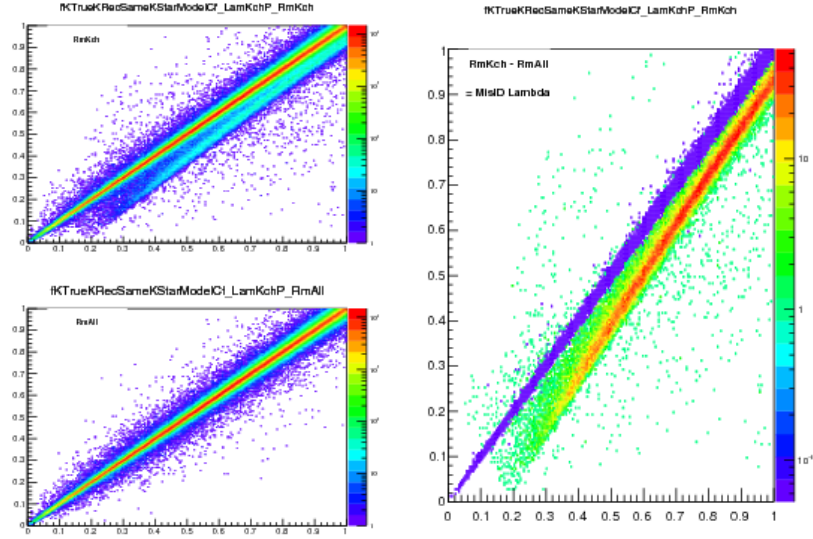
The framework for extracting the necessary transform matrices from the THERMINATOR data is already

(a) Same Event Pairs ( $\Lambda(\bar{\Lambda})K^\pm$ , 0-10% Centrality)(b) Mixed Event Pairs ( $\Lambda(\bar{\Lambda})K^\pm$ , 0-10% Centrality)

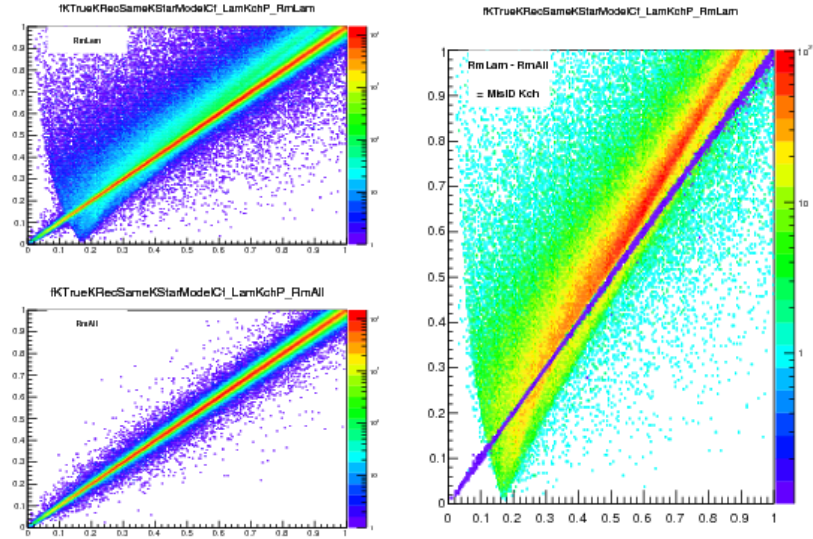
**Fig. 14:** Sample  $k_{True}^*$  vs.  $k_{Rec}^*$  plot for  $\Lambda(\bar{\Lambda})K^\pm$  0-10% analyses. The structure which appears around  $k_{Rec}^* = k_{True}^* - 0.15$  is mainly caused by  $K_S^0$  contamination in our  $\Lambda(\bar{\Lambda})$  sample. The remaining structure not distributed about  $k_{Rec}^* = k_{True}^*$  is due to  $\pi$  and  $e$  contamination in our  $K^\pm$  sample. These contaminations are more clearly visible in Figure 15

in place, and has been used to generate the examples from  $\Lambda K^+$  and  $\bar{\Lambda} K^+$  analyses shown in Figures 16 and 17. However, these residual correlations have not yet been implemented in the fitter.

There is an obvious added complication here, as, for instance, the  $\Xi^- K^\pm$  residuals necessitate the inclusion of the CoulombFitter into the process. The complication of combining the two fitters is not as troubling as the increase in fitting time that this is sure to bring. Additionally, in the future, we may combine our  $\Lambda K$  and  $\Xi K$  analyses to be fit simultaneously.



(a) (Top Left) All misidentified  $K^+$  excluded. (Bottom Left) All misidentified  $\Lambda$  and  $K^+$  excluded. (Right) The difference of (Top Left) - (Bottom Left), which reveals the contamination in our  $\Lambda$  collection. The structure which appears around  $k_{Rec}^* = k_{True}^* - 0.15$  is mainly caused by  $K_S^0$  contamination in our  $\Lambda(\bar{\Lambda})$  sample.



(b) (Top Left) All misidentified  $\Lambda$  excluded. (Bottom Left) All misidentified  $\Lambda$  and  $K^+$  excluded. (Right) The difference of (Top Left) - (Bottom Left), which reveals the contamination in our  $K^+$  collection. The structure not distributed about  $k_{Rec}^* = k_{True}^*$  is due to  $\pi$  and  $e^-$  contamination in our  $K^\pm$  sample.

**Fig. 15:** Note: This is an old figure and is for a small sample of the data. A new version will be generated shortly.  
 $y\text{-axis} = k_{Rec}^*$ ,  $x\text{-axis} = k_{True}^*$ .

(Left)  $k_{Rec}^*$  vs.  $k_{True}^*$  plots for a small sample of the  $\Lambda K^+$  0-10% central analysis, MC truth was used to eliminate misidentified particles in the  $K^+$ (a) and  $\Lambda$ (b) collections. (Right) The difference of the top left and bottom left plots. Contaminations in our particle collections are clearly visible. Figure (a) demonstrates a  $K_S^0$  contamination in our  $\Lambda$  collection; Figure (b) demonstrates a  $\pi$  and  $e^-$  contamination in our  $K^\pm$  collection.

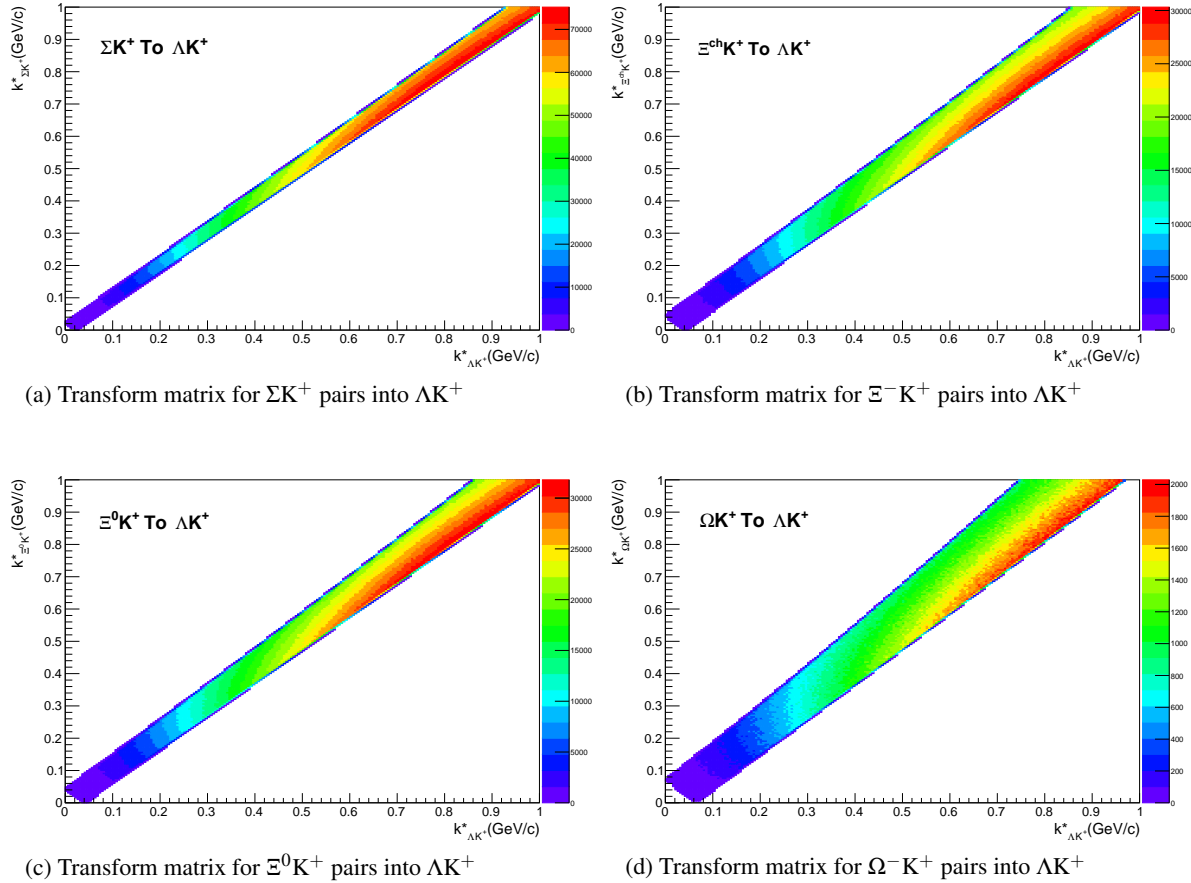


**Fig. 16:** Transform Matrices generated with THERMINATOR for  $\Lambda K^+$  Analysis

## 418 6 Systematic Errors

419 In order to understand my systematic uncertainties, the analysis code was run many times using slightly  
420 different values for a number of important cuts, and the results were compared.

421 In order to quantify the systematic errors on the data, all correlation functions built using all varied cut  
422 values were bin-by-bin averaged, and the resulting variance of each bin was taken as the systematic error.  
423 The cuts which were utilized in this study are presented in Sections 6.1.1 ( $\Lambda K_S^0$ ) and 6.2.1 ( $\Lambda K^\pm$ ).

424 Similarly, the fit parameters extracted from all of these correlation functions were averaged, and the  
425 resulting variances were taken as the systematic errors for the fit parameters. As with the systematic  
426 errors on the data, this was performed for all varied cut values. Additionally, a systematic analysis was  
427 done on our fit method (which, for now, just includes our choice of fit range). These two sources of  
428 uncertainty were combined in quadrature to obtain the final systematic uncertainties on the extracted fit  
429 parameters.

### 430 6.1 Systematic Errors: $\Lambda K_S^0$

#### 431 6.1.1 Particle and Pair Cuts

432 The cuts included in the systematic study, as well as the values used in the variations, are listed below.  
433 Note, the central value corresponds to that used in the analysis.

- 434 1. DCA  $\Lambda(\bar{\Lambda})$ : {4, 5, 6 mm}

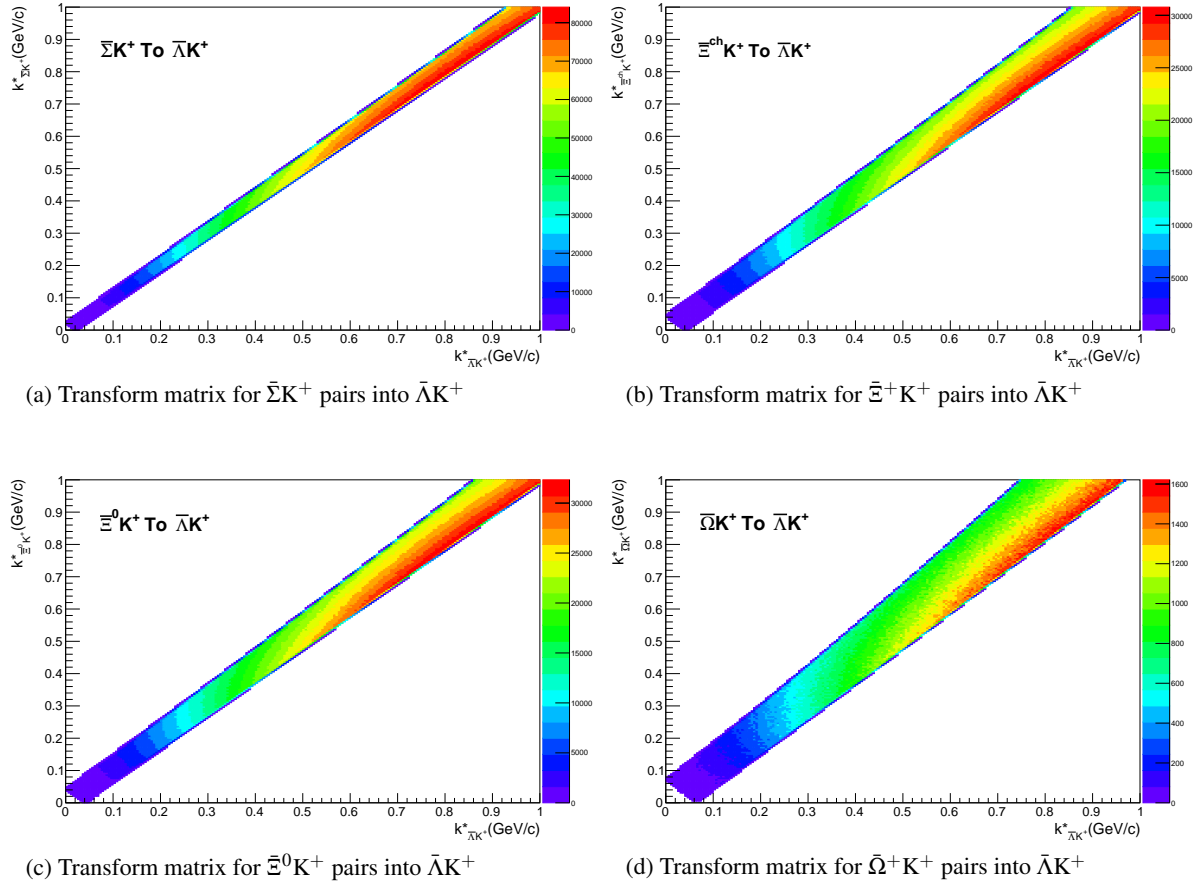


**Fig. 17:** Transform Matrices generated with THERMINATOR for  $\bar{\Lambda}K^+$  Analysis

- 435 2. DCA  $K_S^0$ : {2, 3, 4 mm}
- 436 3. DCA  $\Lambda(\bar{\Lambda})$  Daughters: {3, 4, 5 mm}
- 437 4. DCA  $K_S^0$  Daughters: {2, 3, 4 mm}
- 438 5.  $\Lambda(\bar{\Lambda})$  Cosine of Pointing Angle: {0.9992, 0.9993, 0.9994}
- 439 6.  $K_S^0$  Cosine of Pointing Angle: {0.9992, 0.9993, 0.9994}
- 440 7. DCA to Primary Vertex of  $p(\bar{p})$  Daughter of  $\Lambda(\bar{\Lambda})$ : {0.5, 1, 2 mm}
- 441 8. DCA to Primary Vertex of  $\pi^-(\pi^+)$  Daughter of  $\Lambda(\bar{\Lambda})$ : {2, 3, 4 mm}
- 442 9. DCA to Primary Vertex of  $\pi^+$  Daughter of  $K_S^0$ : {2, 3, 4 mm}
- 443 10. DCA to Primary Vertex of  $\pi^-$  Daughter of  $K_S^0$ : {2, 3, 4 mm}
- 444 11. Average Separation of Like-Charge Daughters: {5, 6, 7 cm}

#### 445 6.1.2 Non-Flat Background

446 Still needs to be done. Currently, we fit our non-flat background with a linear function. We will also use  
447 a quadratic form, and analyze how this choice affects our extracted parameter sets.

---

### 448 **6.1.3 Fit Range**

449 Our choice of  $k^*$  fit range was varied by  $\pm 25\%$ . The resulting uncertainties in the extracted parameter  
450 sets were combined with our uncertainties arising from our particle and pair cuts.

## 451 **6.2 Systematic Errors: $\Lambda K^\pm$**

### 452 **6.2.1 Particle and Pair Cuts**

453 The cuts included in the systematic study, as well as the values used in the variations, are listed below.  
454 Note, the central value corresponds to that used in the analysis.

- 455 1. DCA  $\Lambda(\bar{\Lambda})$ : {4, 5, 6 mm}
- 456 2. DCA  $\Lambda(\bar{\Lambda})$  Daughters: {3, 4, 5 mm}
- 457 3.  $\Lambda(\bar{\Lambda})$  Cosine of Pointing Angle: {0.9992, 0.9993, 0.9994}
- 458 4. DCA to Primary Vertex of  $p(\bar{p})$  Daughter of  $\Lambda(\bar{\Lambda})$ : {0.5, 1, 2 mm}
- 459 5. DCA to Primary Vertex of  $\pi^-(\pi^+)$  Daughter of  $\Lambda(\bar{\Lambda})$ : {2, 3, 4 mm}
- 460 6. Average Separation of  $\Lambda(\bar{\Lambda})$  Daughter with Same Charge as  $K^\pm$ : {7, 8, 9 cm}

### 461 **6.2.2 Non-Flat Background**

462 Still needs to be done. Currently, we fit our non-flat background with a linear function. We will also use  
463 a quadratic form, and analyze how this choice affects our extracted parameter sets.

### 464 **6.2.3 Fit Range**

465 Our choice of  $k^*$  fit range was varied by  $\pm 25\%$ . The resulting uncertainties in the extracted parameter  
466 sets were combined with our uncertainties arising from our particle and pair cuts.

## 467 **6.3 Systematic Errors: $\Xi K^\pm$**

### 468 **6.3.1 Particle and Pair Cuts**

469 The cuts included in the systematic study, as well as the values used in the variations, are listed below.  
470 Note, the central value corresponds to that used in the analysis.

- 471 1. Max. DCA  $\Xi(\bar{\Xi})$ : {x, y, z mm}
- 472 2. Max. DCA  $\Xi(\bar{\Xi})$  Daughters: {x, y, z mm}
- 473 3. Min.  $\Xi(\bar{\Xi})$  Cosine of Pointing Angle to Primary Vertex: {0.9991, 0.9992, 0.9993}
- 474 4. Min.  $\Lambda(\bar{\Lambda})$  Cosine of Pointing Angle to  $\Xi(\bar{\Xi})$  Decay Vertex: {0.9992, 0.9993, 0.9994}
- 475 5. Min. DCA Bachelor  $\pi$ : {0.2, 0.3, 0.4 mm}
- 476 6. Min. DCA  $\Lambda(\bar{\Lambda})$ : {0.5, 1, 2 mm}
- 477 7. Max. DCA  $\Lambda(\bar{\Lambda})$  Daughters: {3, 4, 5 mm}
- 478 8. Min.  $\Lambda(\bar{\Lambda})$  Cosine of Pointing Angle To Primary Vertex: {0.9992, 0.9993, 0.9994}
- 479 9. Min. DCA to Primary Vertex of  $p(\bar{p})$  Daughter of  $\Lambda(\bar{\Lambda})$ : {0.5, 1, 2 mm}

- 480 10. Min. DCA to Primary Vertex of  $\pi^-(\pi^+)$  Daughter of  $\Lambda(\bar{\Lambda})$ : {2, 3, 4 mm}
- 481 11. Min. Average Separation of  $\Lambda(\bar{\Lambda})$  Daughter and  $K^\pm$  with like charge: {7, 8, 9 cm}
- 482 12. Min. Average Separation of Bachelor  $\pi$  and  $K^\pm$  with like charge: {x, y, z cm}
- 483 13. Max. DCA to Primary Vertex in Transverse Plane of  $K^\pm$ : {1.92, 2.4, 2.88}
- 484 14. Max. DCA to Primary Vertex in Longitudinal Direction of  $K^\pm$ : {2.4, 3.0, 3.6}

#### 485 **6.3.2 Non-Flat Background**

486 Still needs to be done. Currently, we fit our non-flat background with a linear function. We will also use  
 487 a quadratic form, and analyze how this choice affects our extracted parameter sets.

#### 488 **6.3.3 Fit Range**

489 Our choice of  $k^*$  fit range was varied by  $\pm 25\%$ . The resulting uncertainties in the extracted parameter  
 490 sets were combined with our uncertainties arising from our particle and pair cuts.

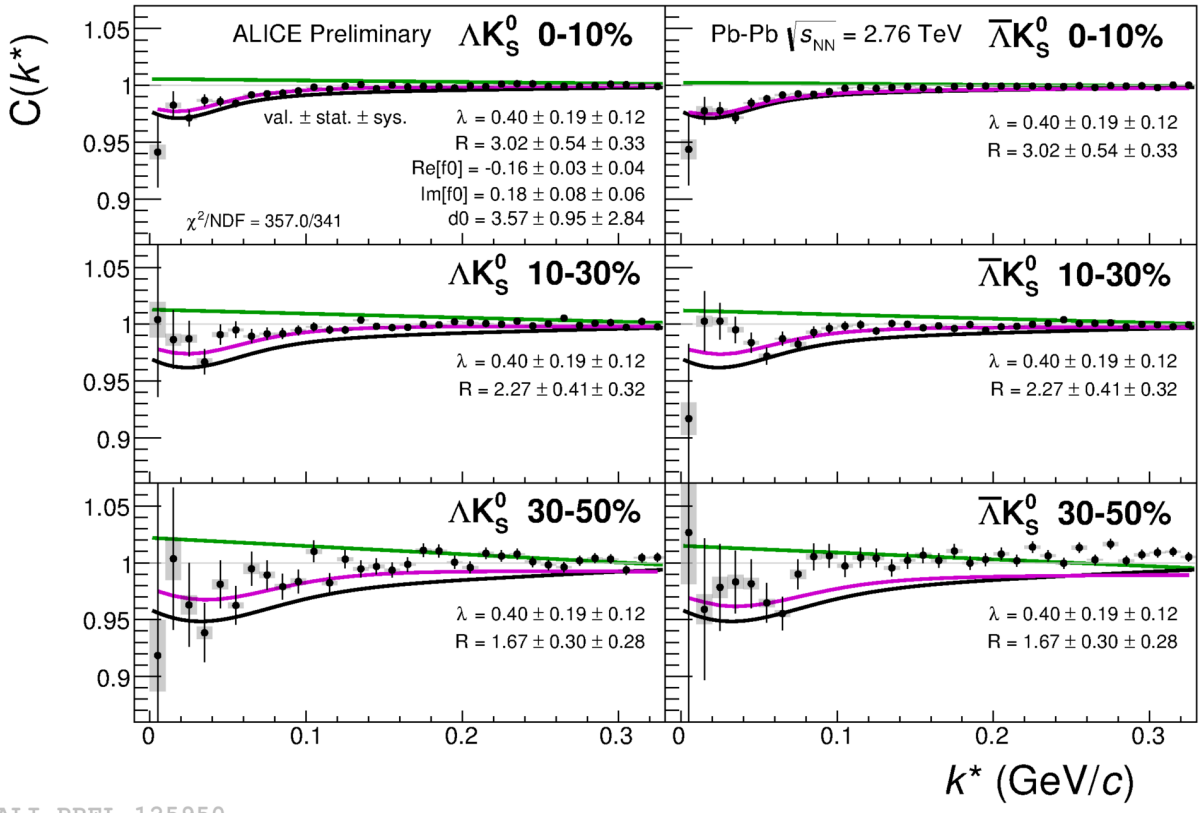
## 491 **7 Results and Discussion**

### 492 **7.1 Results: $\Lambda K_S^0$ and $\Lambda K^\pm$**

493 Figures 18, 20, and 22 (Section 7) show experimental data with fits for all studied centralities for  $\Lambda K_S^0$   
 494 with  $\bar{\Lambda} K_S^0$ ,  $\Lambda K^+$  with  $\bar{\Lambda} K^-$ , and  $\Lambda K^-$  with  $\bar{\Lambda} K^+$ , respectively. The parameter sets extracted from the fits  
 495 can be found in Tables 1 and 2. All correlation functions were normalized in the range  $0.32 < k^* < 0.40$   
 496 GeV/c, and fit in the range  $0.0 < k^* < 0.30$  GeV/c. For the  $\Lambda K^-$  and  $\bar{\Lambda} K^+$  analyses, the region  $0.19$   
 497  $< k^* < 0.23$  GeV/c was excluded from the fit to exclude the bump caused by the  $\Omega^-$  resonance. The  
 498 non-flat background was fit with a linear form from  $0.6 < k^* < 0.9$  GeV/c. The theoretical fit function  
 499 was then multiplied by this background during the fitting process.

500 In the figures (18, 20, and 22), the black solid line represents the “raw” fit, i.e. not corrected for momen-  
 501 tum resolution effects nor non-flat background. The green line shows the fit to the non-flat background.  
 502 The purple points show the fit after momentum resolution and non-flat background corrections have been  
 503 applied. The initial values of the parameters is listed, as well as the final fit values with uncertainties.

504 For the  $\Lambda K_S^0$  fits,  $R$  was restricted to [2.0, 10.0 fm] and  $\Lambda$  was restricted to [0.1, 0.8]. This gave the lowest  
 505  $\chi^2$  value, but loosening this restriction changes the fit parameters slightly. Notice, the 10-30% radius is  
 506 at its limit, as is  $\lambda$  from the 30-50%  $\Lambda K_S^0$  analysis. This accounts for the 0.000 systematic uncertainty of  
 507 the 10-30%  $R$  value currently quoted in Table 1. An estimate for this uncertainty should be included in  
 508 the next version of this note. In the future, we may need to throw out the 30-50% data from the fit, but  
 509 this is not ideal.



ALI-PREL-125950

**Fig. 18:** Fits to the  $\Lambda K_S^0$  (left) and  $\bar{\Lambda} K_S^0$  (right) data for the centralities 0-10% (top), 10-30% (middle), and 30-50% (bottom). The lines represent the statistical errors, while the boxes represent the systematic errors. Each has unique  $\lambda$  and normalization parameters. The radii are shared amongst like centralities; the scattering parameters ( $\text{Re}[f_0]$ ,  $\text{Im}[f_0]$ ,  $d_0$ ) are shared amongst all. The black solid line represents the “raw” fit, i.e. not corrected for momentum resolution effects nor non-flat background. The green line shows the fit to the non-flat background. The purple points show the fit after momentum resolution and non-flat background corrections have been applied. The initial values of the parameters is listed, as well as the final fit values with uncertainties. Here,  $R$  was restricted to [2.,10.] and  $\Lambda$  was restricted to [0.1,0.8].

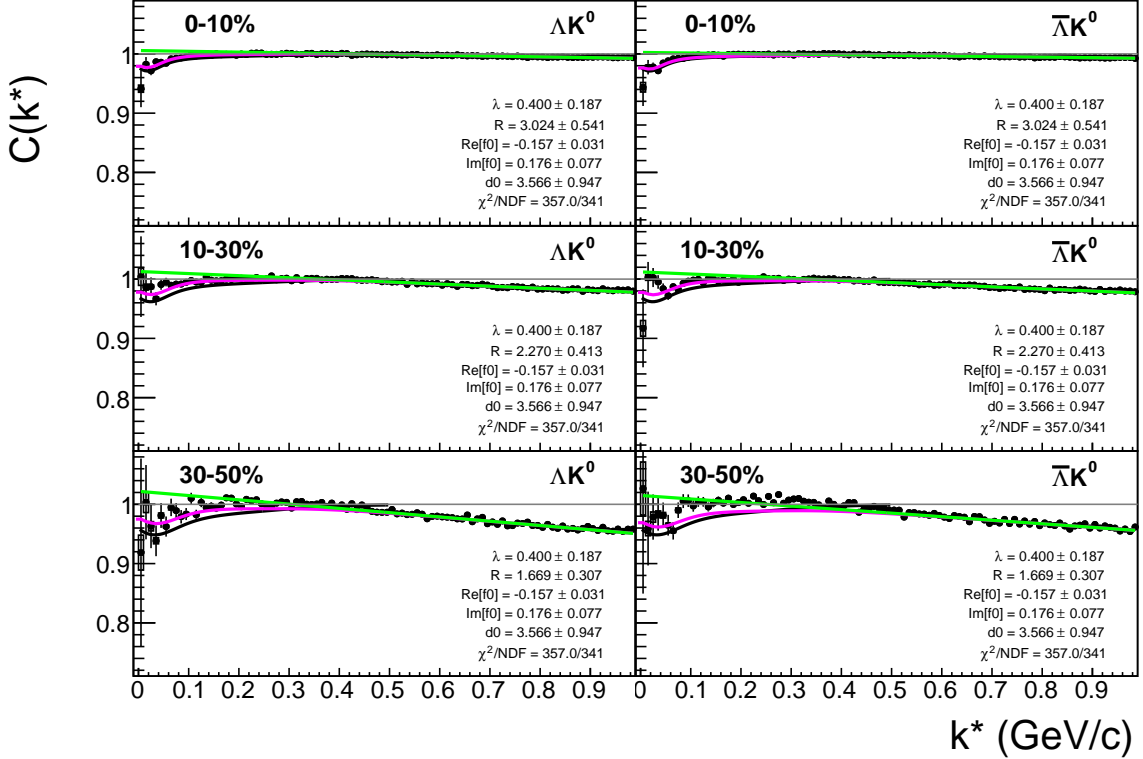
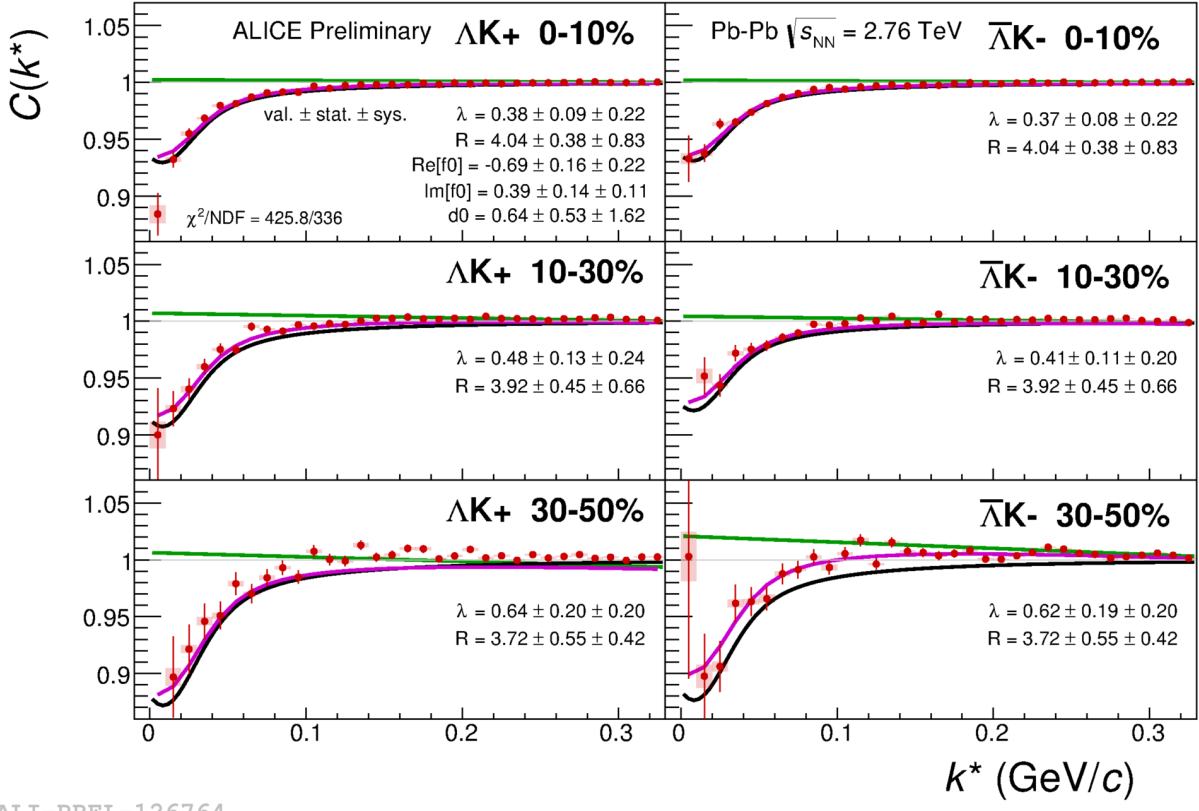


**Fig. 19:** Same as Fig. 18, but with a wider range of view. Fits to the  $\Lambda K_S^0$  (left) and  $\bar{\Lambda} K_S^0$  (right) data for the centralities 0-10% (top), 10-30% (middle), and 30-50% (bottom). The lines represent the statistical errors, while the boxes represent the systematic errors. Each has unique  $\lambda$  and normalization parameters. The radii are shared amongst like centralities; the scattering parameters ( $\mathbb{R}f_0$ ,  $\mathbb{I}f_0$ ,  $d_0$ ) are shared amongst all. The black solid line represents the “raw” fit, i.e. not corrected for momentum resolution effects nor non-flat background. The green line shows the fit to the non-flat background. The purple points show the fit after momentum resolution and non-flat background corrections have been applied. The initial values of the parameters is listed, as well as the final fit values with uncertainties. Here,  $R$  was restricted to [2.,10.] and  $\Lambda$  was restricted to [0.1,0.8].



ALI-PREL-126764

**Fig. 20:** Fits to the  $\Lambda K^+$  (left) and  $\bar{\Lambda} K^-$  (right) data for the centralities 0-10% (top), 10-30% (middle), and 30-50% (bottom). The lines represent the statistical errors, while the boxes represent the systematic errors. Each has unique  $\lambda$  and normalization parameters. The radii are shared amongst like centralities; the scattering parameters ( $Re[f_0]$ ,  $Im[f_0]$ ,  $d_0$ ) are shared amongst all. The black solid line represents the “raw” fit, i.e. not corrected for momentum resolution effects nor non-flat background. The green line shows the fit to the non-flat background. The purple points show the fit after momentum resolution and non-flat background corrections have been applied. The initial values of the parameters is listed, as well as the final fit values with uncertainties.

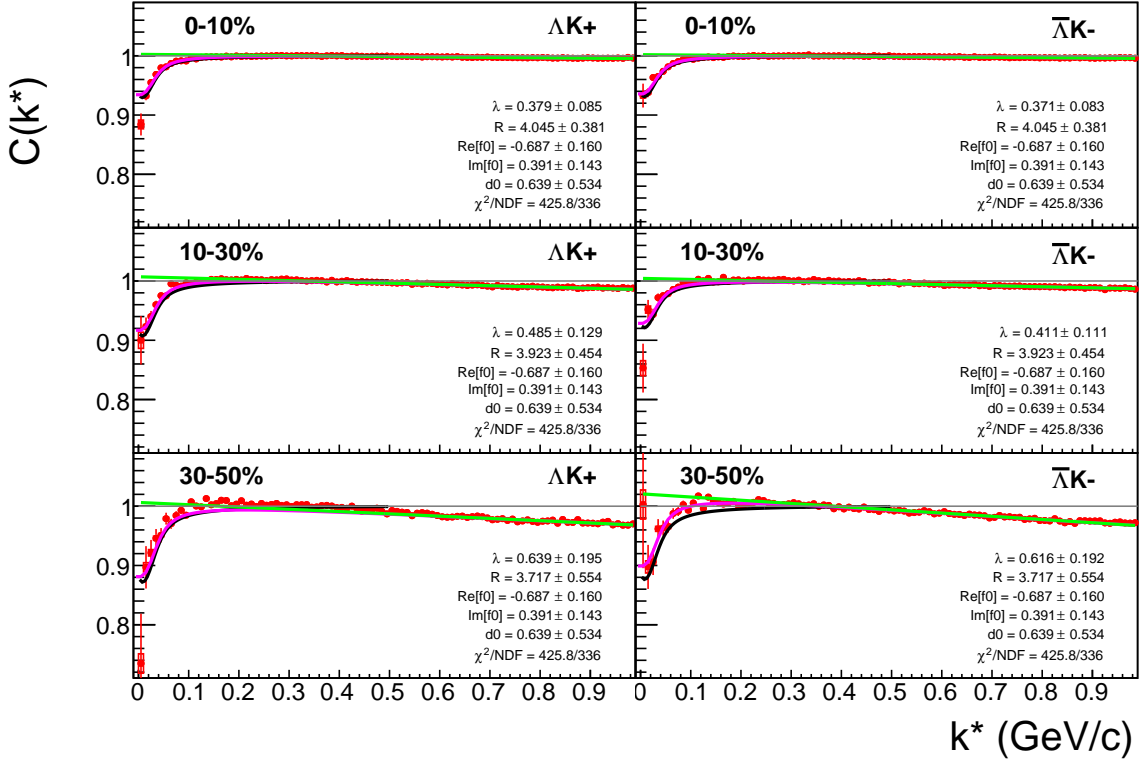


**Fig. 21:** Same as Fig. 20, but with a wider range of view. Fits to the  $\Lambda K^+$  (left) and  $\bar{\Lambda} K^-$  (right) data for the centralities 0-10% (top), 10-30% (middle), and 30-50% (bottom). The lines represent the statistical errors, while the boxes represent the systematic errors. Each has unique  $\lambda$  and normalization parameters. The radii are shared amongst like centralities; the scattering parameters ( $\mathbb{R} f_0$ ,  $\mathbb{I} f_0$ ,  $d_0$ ) are shared amongst all. The black solid line represents the “raw” fit, i.e. not corrected for momentum resolution effects nor non-flat background. The green line shows the fit to the non-flat background. The purple points show the fit after momentum resolution and non-flat background corrections have been applied. The initial values of the parameters is listed, as well as the final fit values with uncertainties.

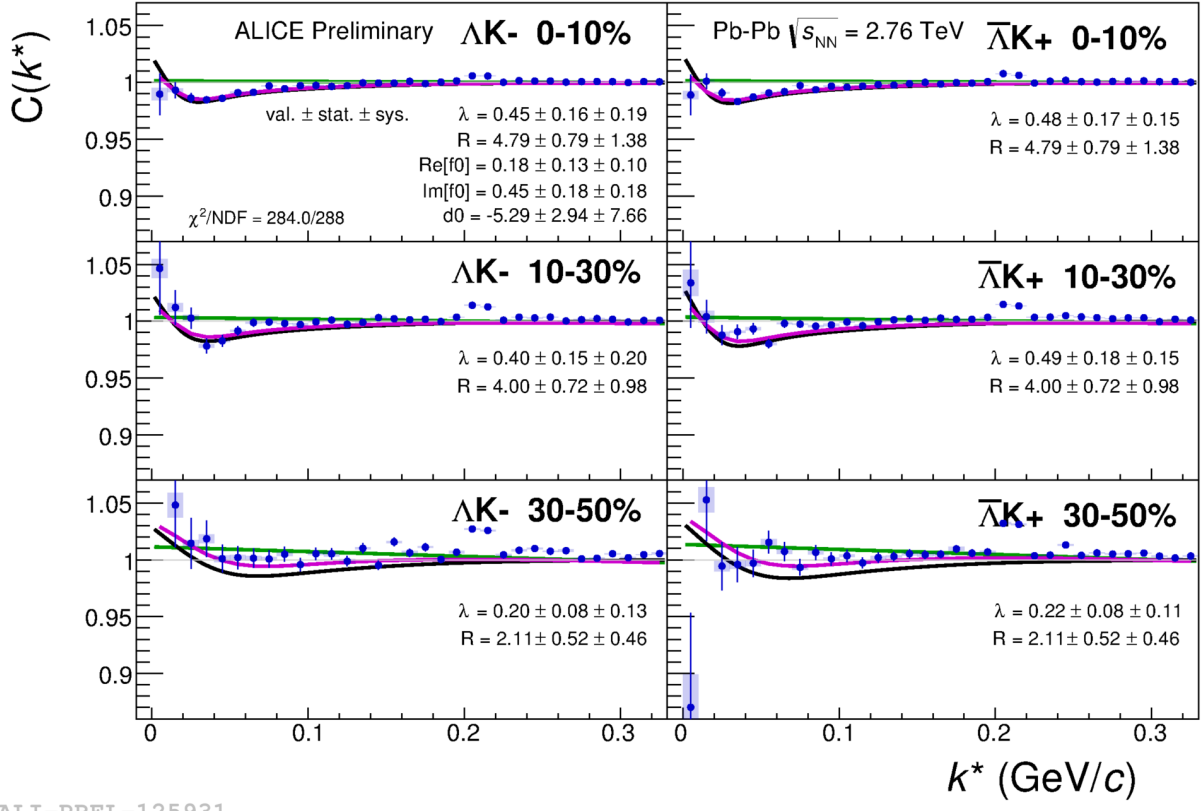


**Fig. 22:** Fits to the  $\Lambda K^-$  (left) with  $\bar{\Lambda} K^+$  (right) data for the centralities 0-10% (top), 10-30% (middle), and 30-50% (bottom). The lines represent the statistical errors, while the boxes represent the systematic errors. Each has unique  $\lambda$  and normalization parameters. The radii are shared amongst like centralities; the scattering parameters ( $\text{Re}[f_0]$ ,  $\text{Im}[f_0]$ ,  $d_0$ ) are shared amongst all. The black solid line represents the “raw” fit, i.e. not corrected for momentum resolution effects nor non-flat background. The green line shows the fit to the non-flat background. The purple points show the fit after momentum resolution and non-flat background corrections have been applied. The initial values of the parameters is listed, as well as the final fit values with uncertainties.

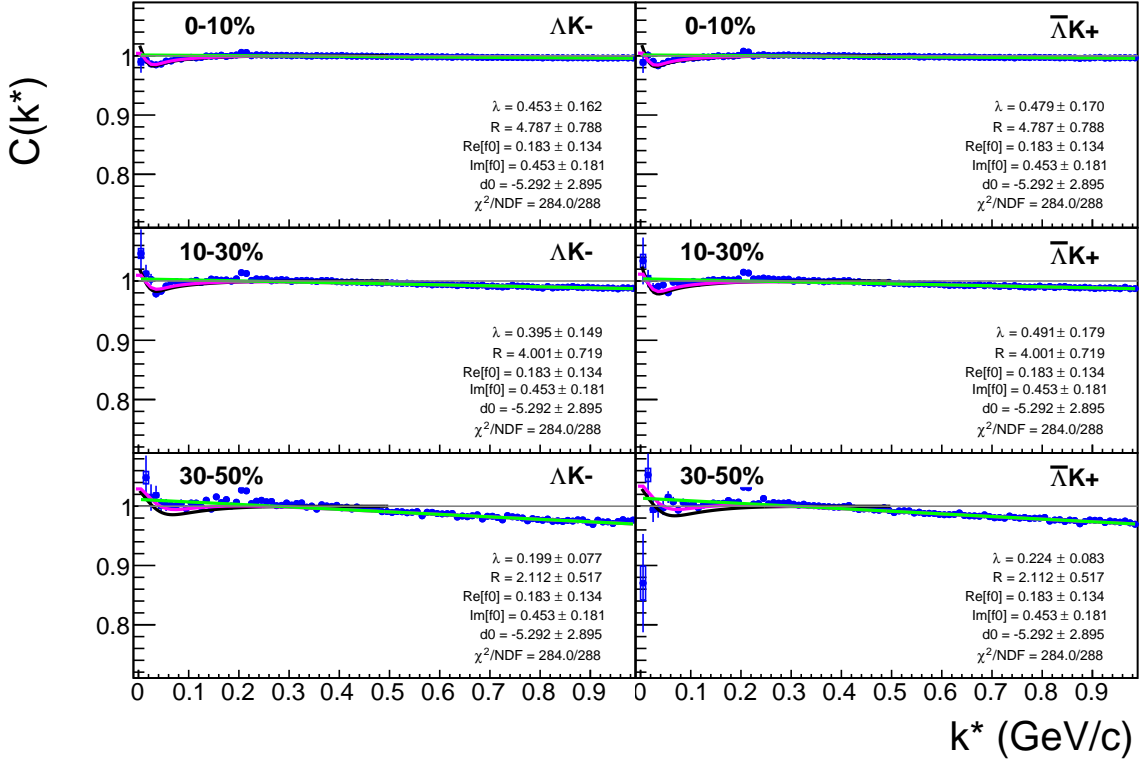


**Fig. 23:** Same as Fig. 22, but with a wider range of view. Fits to the  $\Lambda K^-$  (left) with  $\bar{\Lambda} K^+$  (right) data for the centralities 0-10% (top), 10-30% (middle), and 30-50% (bottom). The lines represent the statistical errors, while the boxes represent the systematic errors. Each has unique  $\lambda$  and normalization parameters. The radii are shared amongst like centralities; the scattering parameters ( $\mathbb{R} f_0$ ,  $\mathbb{I} f_0$ ,  $d_0$ ) are shared amongst all. The black solid line represents the “raw” fit, i.e. not corrected for momentum resolution effects nor non-flat background. The green line shows the fit to the non-flat background. The purple points show the fit after momentum resolution and non-flat background corrections have been applied. The initial values of the parameters is listed, as well as the final fit values with uncertainties.

Fit Results $\Lambda(\bar{\Lambda})K_S^0$						
Pair Type	Centrality	Fit Parameters				
		$\lambda$	$R$	$\mathbb{R}f_0$	$\mathbb{I}f_0$	$d_0$
$\Lambda K_S^0$	0-10%	$0.400 \pm 0.187$ (stat.) $\pm 0.116$ (sys.)	$3.024 \pm 0.541$ (stat.) $\pm 0.329$ (sys.)	$-0.157 \pm 0.031$ (stat.) $\pm 0.043$ (sys.)	$0.176 \pm 0.077$ (stat.) $\pm 0.059$ (sys.)	$3.566 \pm 0.947$ (stat.) $\pm 2.836$ (sys.)
	10-30%		$2.270 \pm 0.413$ (stat.) $\pm 0.324$ (sys.)			
	30-50%		$1.669 \pm 0.307$ (stat.) $\pm 0.280$ (sys.)			
$\bar{\Lambda} K_S^0$	0-10%	$0.400 \pm 0.187$ (stat.) $\pm 0.116$ (sys.)	$3.024 \pm 0.541$ (stat.) $\pm 0.329$ (sys.)	$-0.157 \pm 0.031$ (stat.) $\pm 0.043$ (sys.)	$0.176 \pm 0.077$ (stat.) $\pm 0.059$ (sys.)	$3.566 \pm 0.947$ (stat.) $\pm 2.836$ (sys.)
	10-30%		$2.270 \pm 0.413$ (stat.) $\pm 0.324$ (sys.)			
	30-50%		$1.669 \pm 0.307$ (stat.) $\pm 0.280$ (sys.)			

**Table 1:** Fit Results  $\Lambda(\bar{\Lambda})K_S^0$ . Each pair is fit simultaneously with its conjugate (ie.  $\Lambda K_S^0$  with  $\bar{\Lambda} K_S^0$ ) across all centralities (0-10%, 10-30%, 30-50%), for a total of 6 simultaneous analyses in the fit. Each analysis has a unique  $\lambda$  and normalization parameter. The radii are shared between analyses of like centrality, as these should have similar source sizes. The scattering parameters ( $\mathbb{R}f_0$ ,  $\mathbb{I}f_0$ ,  $d_0$ ) are shared amongst all. The fit is done on the data with only statistical error bars. The errors marked as “stat.” are those returned by MINUIT. The errors marked as “sys.” are those which result from my systematic analysis (as outlined in Section 6).

Fit Results $\Lambda(\bar{\Lambda})K^\pm$						
Pair Type	Centrality	Fit Parameters				
		$\lambda$	$R$	$\mathbb{R}f_0$	$\mathbb{I}f_0$	$d_0$
$\Lambda K^+$	0-10%	$0.379 \pm 0.085$ (stat.) $\pm 0.220$ (sys.)	$4.045 \pm 0.381$ (stat.) $\pm 0.830$ (sys.)	$-0.687 \pm 0.160$ (stat.) $\pm 0.223$ (sys.)	$0.391 \pm 0.143$ (stat.) $\pm 0.111$ (sys.)	$0.639 \pm 0.534$ (stat.) $\pm 1.621$ (sys.)
	10-30%	$0.485 \pm 0.129$ (stat.) $\pm 0.241$ (sys.)	$3.923 \pm 0.454$ (stat.) $\pm 0.663$ (sys.)			
	30-50%	$0.639 \pm 0.195$ (stat.) $\pm 0.204$ (sys.)	$3.717 \pm 0.554$ (stat.) $\pm 0.420$ (sys.)			
$\bar{\Lambda} K^-$	0-10%	$0.371 \pm 0.083$ (stat.) $\pm 0.217$ (sys.)	$4.045 \pm 0.381$ (stat.) $\pm 0.830$ (sys.)	$0.183 \pm 0.134$ (stat.) $\pm 0.095$ (sys.)	$0.453 \pm 0.181$ (stat.) $\pm 0.184$ (sys.)	$-5.292 \pm 2.895$ (stat.) $\pm 7.658$ (sys.)
	10-30%	$0.411 \pm 0.111$ (stat.) $\pm 0.201$ (sys.)	$3.923 \pm 0.454$ (stat.) $\pm 0.663$ (sys.)			
	30-50%	$0.616 \pm 0.192$ (stat.) $\pm 0.203$ (sys.)	$3.717 \pm 0.554$ (stat.) $\pm 0.420$ (sys.)			
$\Lambda K^-$	0-10%	$0.453 \pm 0.162$ (stat.) $\pm 0.186$ (sys.)	$4.787 \pm 0.788$ (stat.) $\pm 1.375$ (sys.)	$0.183 \pm 0.134$ (stat.) $\pm 0.095$ (sys.)	$0.453 \pm 0.181$ (stat.) $\pm 0.184$ (sys.)	$-5.292 \pm 2.895$ (stat.) $\pm 7.658$ (sys.)
	10-30%	$0.395 \pm 0.149$ (stat.) $\pm 0.198$ (sys.)	$4.001 \pm 0.719$ (stat.) $\pm 0.978$ (sys.)			
	30-50%	$0.199 \pm 0.077$ (stat.) $\pm 0.132$ (sys.)	$2.112 \pm 0.517$ (stat.) $\pm 0.457$ (sys.)			
$\bar{\Lambda} K^+$	0-10%	$0.479 \pm 0.170$ (stat.) $\pm 0.152$ (sys.)	$4.787 \pm 0.788$ (stat.) $\pm 1.375$ (sys.)	$0.183 \pm 0.134$ (stat.) $\pm 0.095$ (sys.)	$0.453 \pm 0.181$ (stat.) $\pm 0.184$ (sys.)	$-5.292 \pm 2.895$ (stat.) $\pm 7.658$ (sys.)
	10-30%	$0.491 \pm 0.179$ (stat.) $\pm 0.148$ (sys.)	$4.001 \pm 0.719$ (stat.) $\pm 0.978$ (sys.)			
	30-50%	$0.224 \pm 0.083$ (stat.) $\pm 0.106$ (sys.)	$2.112 \pm 0.517$ (stat.) $\pm 0.457$ (sys.)			

**Table 2:** Fit Results  $\Lambda(\bar{\Lambda})K^\pm$  Each pair is fit simultaneously with its conjugate (ie.  $\Lambda K^+$  with  $\bar{\Lambda} K^-$  and  $\Lambda K^-$  with  $\bar{\Lambda} K^+$ ) across all centralities (0-10%, 10-30%, 30-50%), for a total of 6 simultaneous analyses in the fit. Each analysis has a unique  $\lambda$  and normalization parameter. The radii are shared between analyses of like centrality, as these should have similar source sizes. The scattering parameters ( $\mathbb{R}f_0$ ,  $\mathbb{I}f_0$ ,  $d_0$ ) are shared amongst all. The fit is done on the data with only statistical error bars. The errors marked as “stat.” are those returned by MINUIT. The errors marked as “sys.” are those which result from my systematic analysis (as outlined in Section 6).

**Fit Parameters (value  $\pm$  statistical error  $\pm$  systematic error)**

Pair Type	Centrality	R		
		$\Re f_0$	$\Im f_0$	$d_0$
$\Lambda K^+ & \bar{\Lambda} K^-$	0-10%		<b><math>4.04 \pm 0.38 \pm 0.83</math></b>	
	10-30%		<b><math>3.92 \pm 0.45 \pm 0.66</math></b>	
	30-50%		<b><math>3.72 \pm 0.55 \pm 0.42</math></b>	
		<b><math>-0.69 \pm 0.16 \pm 0.22</math></b>	<b><math>0.39 \pm 0.14 \pm 0.11</math></b>	<b><math>0.64 \pm 0.53 \pm 1.62</math></b>
$\Lambda K^- & \bar{\Lambda} K^+$	0-10%		<b><math>4.79 \pm 0.79 \pm 1.38</math></b>	
	10-30%		<b><math>4.00 \pm 0.72 \pm 0.98</math></b>	
	30-50%		<b><math>2.11 \pm 0.52 \pm 0.46</math></b>	
		<b><math>0.18 \pm 0.13 \pm 0.10</math></b>	<b><math>0.45 \pm 0.18 \pm 0.18</math></b>	<b><math>-5.29 \pm 2.94 \pm 7.66</math></b>
$\Lambda K_S^0 & \bar{\Lambda} K_S^0$	0-10%		<b><math>3.02 \pm 0.54 \pm 0.33</math></b>	
	10-30%		<b><math>2.27 \pm 0.41 \pm 0.32</math></b>	
	30-50%		<b><math>1.67 \pm 0.30 \pm 0.28</math></b>	
		<b><math>-0.16 \pm 0.03 \pm 0.04</math></b>	<b><math>0.18 \pm 0.08 \pm 0.06</math></b>	<b><math>3.57 \pm 0.95 \pm 2.84</math></b>

## 510 7.2 Results: $\Xi K^\pm$

511 Preliminary results and fits for our  $\Xi K^\pm$  analyses are expected to be uploaded by 16 December 2016.  
 512 Even without any fits to the data, the fact that the  $\Xi^- K^+$  data dips below unity is exciting, as this cannot  
 513 occur purely from a Coulomb interaction. We hope that this dip signifies that we are able to peer through  
 514 the overwhelming contribution from the Coulomb interaction to see the effects arising from the strong  
 515 interaction.

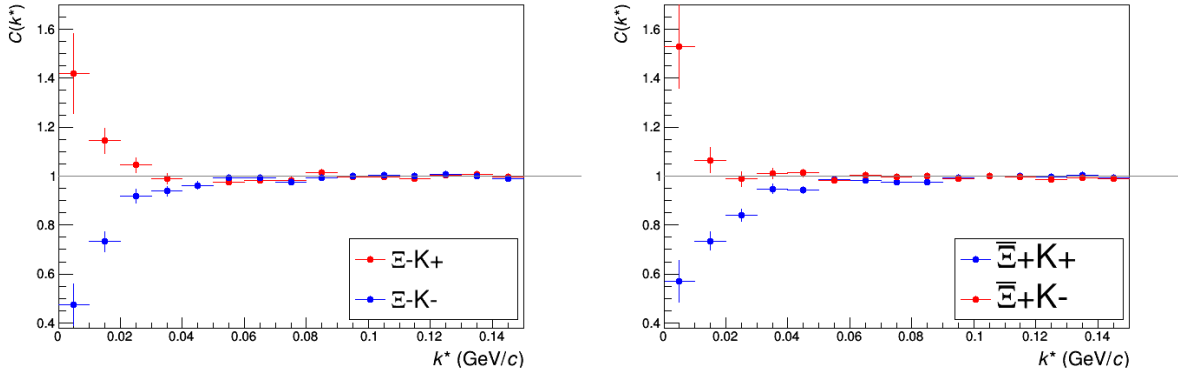
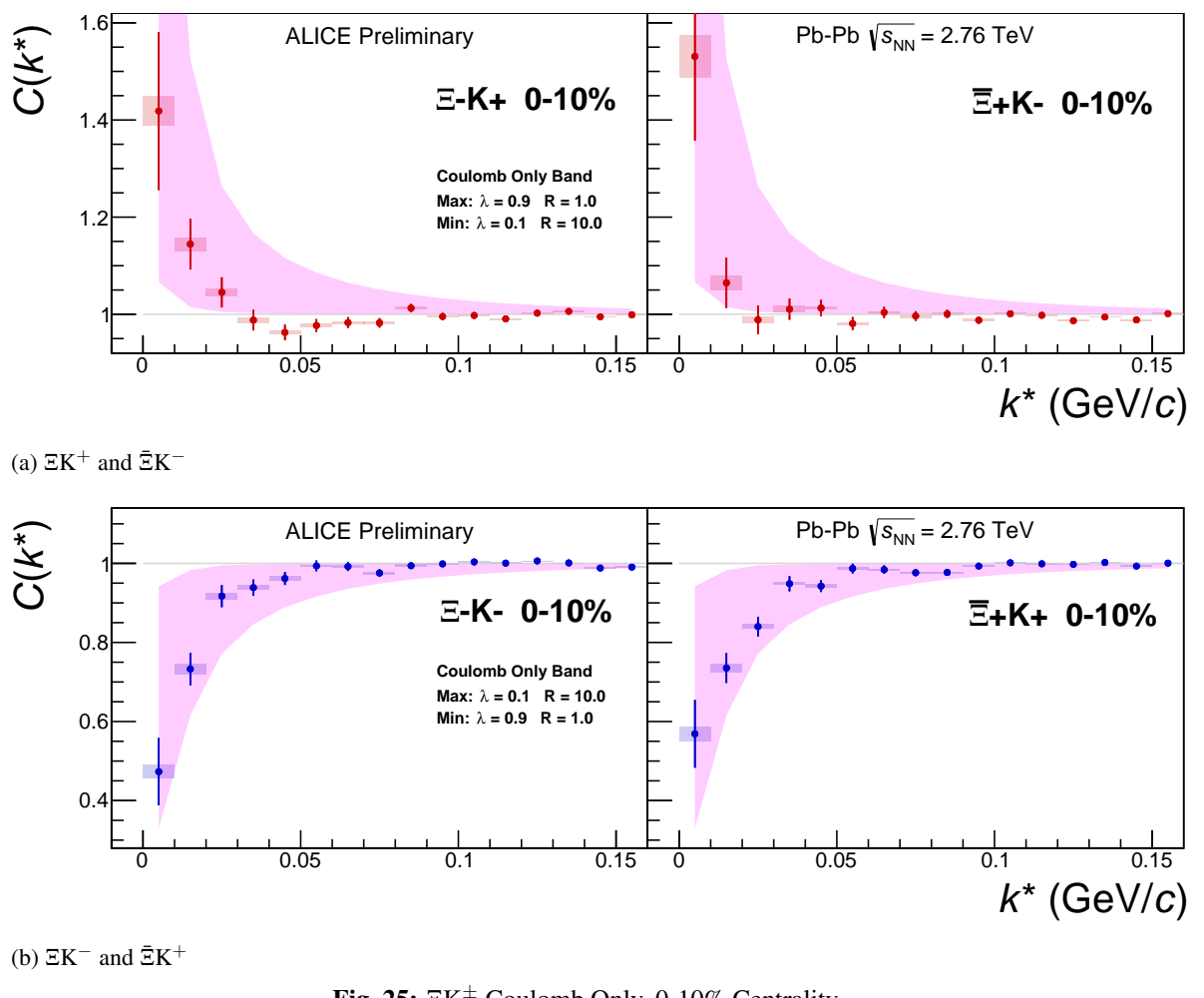


Fig. 24:  $\Xi K^\pm$  Results for 0-10% Centrality

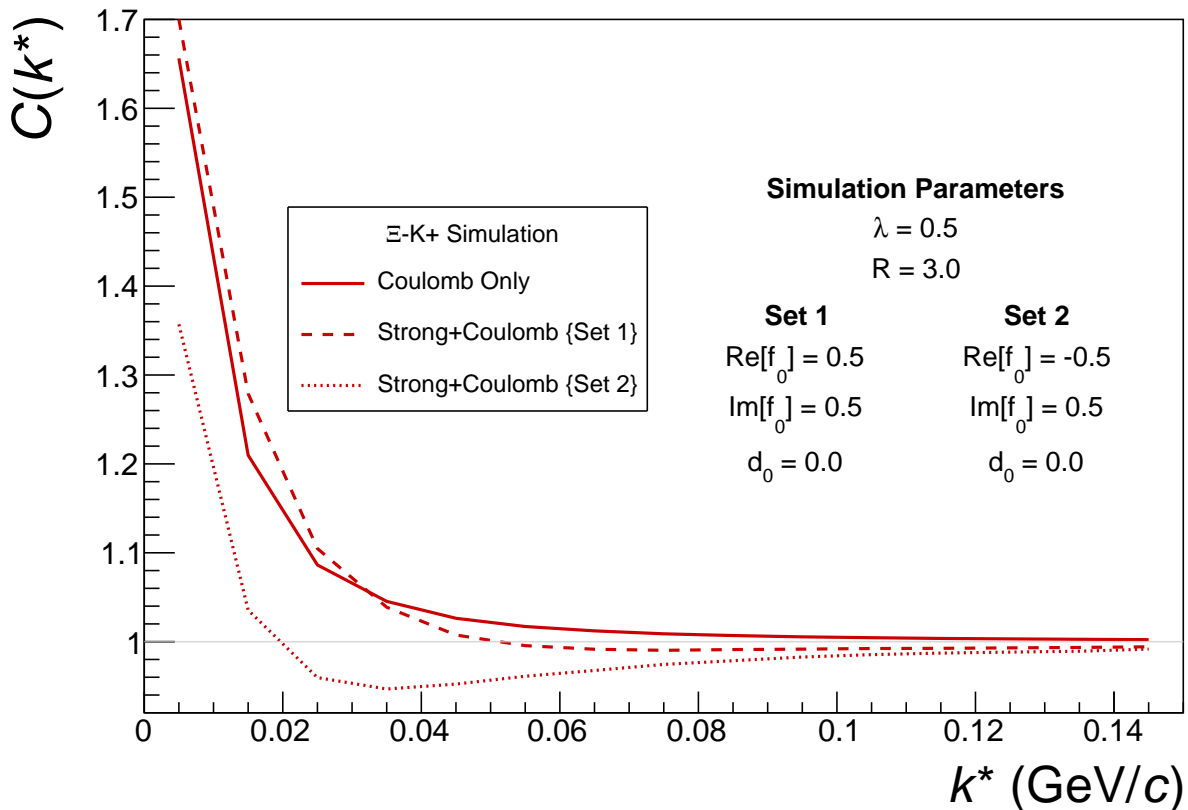
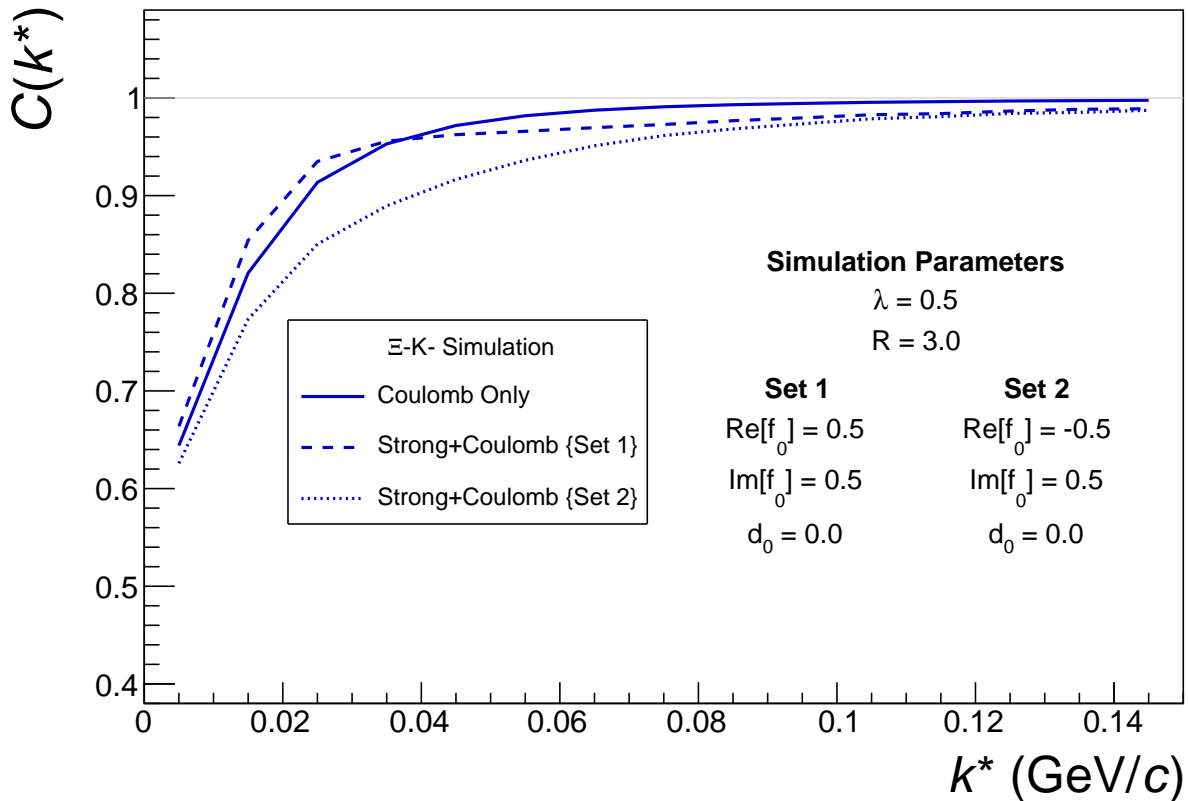
## 516 8 To Do

### References

- [1] R. Lednicky and V. L. Lyuboshitz. *Sov. J. Nucl. Phys.*, 35:770, 1982.
- [2] Michael Annan Lisa, Scott Pratt, Ron Soltz, and Urs Wiedemann. Femtoscopy in relativistic heavy ion collisions. *Ann. Rev. Nucl. Part. Sci.*, 55:357–402, 2005.
- [3] Richard Lednicky. Finite-size effects on two-particle production in continuous and discrete spectrum. *Phys. Part. Nucl.*, 40:307–352, 2009.



**Fig. 25:**  $\Xi K^\pm$  Coulomb Only, 0-10% Centrality

(a)  $\Xi K^+$  and  $\bar{\Xi} K^-$ (b)  $\Xi K^-$  and  $\bar{\Xi} K^+$ **Fig. 26:**  $\Xi K^\pm$  Coulomb Only, 0-10% Centrality